

Bow shocks, bow waves, and dust waves

William J. Henney, S. Jane Arthur, & Jorge A. Tarango-Yong

Instituto de Radioastronomía y Astrofísica, Universidad Nacional Autónoma de México, Apartado Postal 3-72, 58090 Morelia, Michoacán, México

Accepted XXX. Received YYY; in original form ZZZ

ABSTRACT

Dust waves and bow waves result from the action of a star’s radiation pressure on a stream of dust grains that is flowing past it. They are an alternative mechanism to hydrodynamic bow shocks for explaining the curved arcs of infrared emission seen around some stars. We employ simple cylindrically symmetric models for the dust grain dynamics under the influence of radiation and weak gas–grain coupling, which produce bow shapes that we call dragoids. We also show how thin-shell hydrodynamic models can be modified to treat the case of strong gas-grain coupling, producing bow shapes that we call trapoids. Using our recently developed two-dimensional classification scheme for projected bow shapes, we then analyze the inclination-dependent tracks of the dragoids and trapoids in the planitude–alatitude plane, finding interesting differences from the wilkinoid, cantoid, and ancantoid shapes of hydrodynamic bow shock models. We further show how these are modified in the presence of small-amplitude standing-wave oscillations of the basic shape, as may be produced by hydrodynamic instabilities or a time-varying source. We analyze the prospects of using shape analysis of observational datasets to discriminate between different bow models, finding that sample sizes of order 100 are required.

Key words: circumstellar matter – radiation: dynamics – stars: winds, outflows

1 INTRODUCTION

Curved emission arcs around stars (e.g., Gull & Sofia 1979) are often interpreted as *bow shocks*, due to a supersonic hydrodynamic interaction between the star’s wind and an external stream. This stream may be due to the star’s own motion or to an independent flow, such as an H II region in the champagne phase (Tenorio-Tagle 1979), or another star’s wind (Canto et al. 1996). However, an alternative interpretation in some cases may be a radiation-pressure driven bow wave, as first proposed by van Buren & McCray (1988, §vi). In this scenario, photons emitted by the star are absorbed by dust grains in the incoming stream, with the resultant momentum transfer being sufficient to decelerate and deflect the grains within a certain distance from the star, forming a dust-free, bow-shaped cavity with an enhanced dust density at its edge. Two regimes are possible, depending on the strength of coupling between the gas (or plasma) and the dust. In the strong-coupling regime, gas–grain drag decelerates the gas along with the dust, forming a shocked gas shell in a similar fashion to the wind-driven bow shock case. In the weak-coupling regime, the gas stream is relatively unaffected and the dust temporarily decouples to form a dust-only shell. This second case has recently been studied in detail in the context of the interaction of late O-type stars (which have only weak stellar winds) with dusty photoevaporation flows inside H II regions (Ochsendorf et al. 2014b,a; Ochsendorf & Tielens 2015). We follow the nomenclature proposed by Ochsendorf et al. (2014a), in which *dust wave* refers to the weak coupling case and *bow wave* to the strong coupling case. More complex, hybrid scenarios are also possible, such as that

studied by van Marle et al. (2011), where a hydrodynamic bow shock forms, but the larger dust grains that accompany the stellar wind pass right through the shocked gas shell, and form their own dust wave at a larger radius.

In Tarango Yong & Henney (2018, hereafter Paper I), we proposed a new two-dimensional classification scheme for bow shapes: the projected planitude–alatitude, or $\Pi' - \Lambda'$, diagram. Planitude measures the flatness of the bow’s apex, while alatitude measures the openness of the bow’s wings. Both are dimensionless ratios of lengths that can be estimated from observational images. We have analyzed the inclination-dependent tracks on the $\Pi' - \Lambda'$ plane for simple geometric shapes (spheroids, paraboloids, hyperboloids) and for thin-shell hydrodynamic bow shock models (wilkinoid, cantoids, ancantoids). In this paper, we will do the same for simple models of radiation-driven dust waves (dragoids) and bow waves (trapoids).

The paper is organized as follows. In § ?? we do the same for simple models of a dusty radiation bow wave (dragoids), including the effects of gas–grain drag. In § 4 we investigate the effects on the planitude–alatitude plane of small-amplitude perturbations to the bow shape.

2 DIFFERENT TYPES OF BOW

In this section, we investigate the different types of bow interaction that will occur in different regions of parameter space. We will

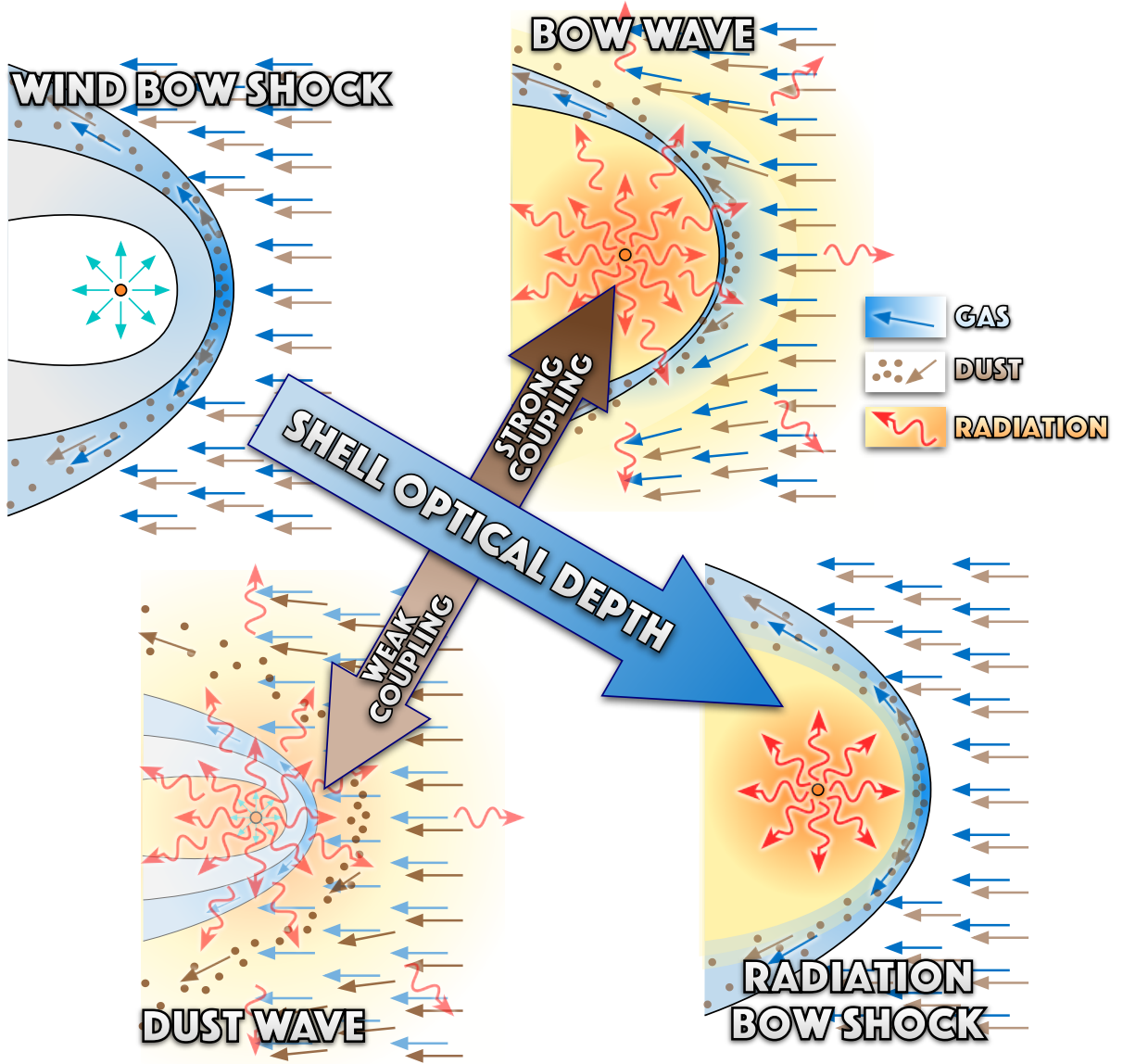


Figure 1. Bow shocks, bow waves, and dust waves

mainly treat the canonical case¹ of a bow around a star of bolometric luminosity, L , with a radiatively driven wind, which is immersed in an external stream of gas and dust with density, ρ , and velocity, v . The size and shape of the bow is determined by a generalized balance of pressure (or, equivalently, momentum) between internal and external sources. We assume that the stream is supersonic and super-alfvenic, so that the external pressure is dominated by the ram pressure: ρv^2 .

¹ Variant cases with differing arrangements of dust and radiation sources are treated in § 3.

2.1 Strong gas-grain coupling

We first consider the case where the dust grains and gas are perfectly coupled by collisions.² Although dust grains typically constitute only a small fraction $Z_d \sim 0.01$ of the mass of the external stream, they nevertheless dominate the broad-band opacity at FUV, optical and

² Cases where this assumption does not hold are investigated below in § 2.2.



Figure 2. Bow regimes in parameter space (v, n) of the external stream for main-sequence OB stars of different masses: (a) $10 M_{\odot}$, (b) $20 M_{\odot}$, (c) $40 M_{\odot}$. In all cases, $\kappa = 600 \text{ cm}^2 \text{ g}^{-1}$ and efficient gas-grain coupling is assumed. Solid black lines of varying width show the bow size (star-apex separation, R_0), while gray shading shows the radiation bow wave regime, with lower border $\tau = \eta$ and upper border $\tau = 1$, where $\tau = 2\kappa\rho R_0$ is the optical depth through the bow. For bows above the red solid line, the ionization front is trapped inside the bow. Blue lines delineate different cooling regimes. Above the thin blue line ($d_{\text{cool}} = h_0$), the bow shock radiates efficiently, forming a thin shocked shell. Below the thick blue line ($d_{\text{cool}} = R_0$), the bow shock is essentially non-radiative.

IR wavelengths if they are present.³ The strong coupling assumption means that all the radiative forces applied to the dust grains are directly felt by the gas also.

2.1.1 Bows supported by radiation and wind

The internal pressure is the sum of wind ram pressure and the effective radiation pressure that acts on the bow shell. The radiative momentum loss rate of the star is L/c and the wind momentum loss rate can be expressed as

$$\dot{M}V = \eta L/c, \quad (1)$$

where η is the momentum efficiency of the wind, which is typically < 1 (Lamers & Cassinelli 1999). If the optical depth is very large, then all of the stellar radiative momentum, emitted with rate L/c , is trapped by the bow shell. In the single scattering limit,⁴ and temporarily neglecting the wind, then pressure balance at the bow apex, a distance R_0 along the symmetry axis from the star is given

³ At EUV wavelengths ($\lambda < 912 \text{ \AA}$), gas opacity dominates if the hydrogen neutral fraction is larger than ≈ 0.001 , see discussion of ionization front trapping below.

⁴ Although it may seem inconsistent to assume single scattering in the case of high optical depths, this is defensible for the following reasons. (1) The grain albedo is not that high (typically ~ 0.5 at ultraviolet through optical wavelengths). (2) The scattered radiation field is more isotropic than the stellar field, leading to cancellation in the radiative flux. (3) Absorbed radiation is re-emitted at infrared wavelengths, where the dust opacity is very much lower.

by

$$\frac{L}{4\pi c R_0^2} = \rho v^2, \quad (2)$$

which yields a fiducial bow shock radius in this optically thick limit as

$$R_* = \left(\frac{L}{4\pi c \rho v^2} \right)^{1/2}. \quad (3)$$

We now consider the opposite, optically thin limit. If the total opacity (gas plus dust) per total mass (gas plus dust) is κ (with units of $\text{cm}^2 \text{ g}^{-1}$), then the radiative acceleration is

$$a_{\text{rad}} = \frac{\kappa L}{4\pi c R^2}. \quad (4)$$

Therefore, an incoming stream with initial velocity, v_∞ , can be brought to rest by radiation alone⁵ at a distance R_0 where

$$\int_{R_0}^{\infty} a_{\text{rad}} dr = \frac{1}{2} v_\infty^2, \quad (5)$$

yielding

$$R_0 = \frac{\kappa L}{2\pi c v_\infty^2}. \quad (6)$$

On the other hand, we can also argue as in the optically thick case

⁵ For simplicity, we here ignore the effects of gravity, which are important for low ratios of $\kappa L/M$, see § 2.1.2. We also ignore pressure gradients and shocks, which are important as the velocity approaches the sound speed, c_s (in § XX below, we show that the resultant corrections to R_0 are of order c_s/v_∞).

4 Henney, Arthur, & Tarango Yong

above by approximating the bow shell as a surface, and balancing stellar radiation pressure against the ram pressure of the incoming stream. The important difference when the shell is not optically thick is that only a fraction $1 - e^{-\tau}$ of the radiative momentum is absorbed by the bow, so that equation (2) is replaced with

$$\frac{L(1 - e^{-\tau})}{4\pi c R_0^2} = \rho v^2. \quad (7)$$

In the optically thin limit, $1 - e^{-\tau} \approx \tau$, so these two descriptions can be seen to agree so long as

$$\tau = 2\kappa\rho R_0, \quad (8)$$

which we will assume to hold generally.

Then, defining a fiducial optical depth,

$$\tau_* = \rho\kappa R_*, \quad (9)$$

and adding in the stellar wind ram pressure⁶ from equation (1), we find that the general bow radius can be written in terms of the fiducial radius as $R_0 = xR_*$, where x is the solution of

$$x^2 - (1 - e^{-2\tau_* x}) - \eta = 0. \quad (10)$$

Since this is a transcendental equation, x must be found numerically, but we can write explicit expressions for three limiting cases:

$$x \approx \begin{cases} \text{if } \tau_* \gg 1: & (1 + \eta)^{1/2} \\ \text{if } \tau_*^2 \ll 1: & \tau_* + (\tau_*^2 + \eta)^{1/2} \approx \begin{cases} \text{if } \tau_*^2 \gg \eta: & 2\tau_* \\ \text{if } \tau_*^2 \ll \eta: & \eta^{1/2} \end{cases} \end{cases} \quad (11)$$

The first case, $x \approx (1 + \eta)^{1/2}$, corresponds to a *radiation bow shock*; the second case, $x \approx 2\tau_*$, corresponds to a *radiation bow wave*; and the third case, $x \approx \eta^{1/2}$, corresponds to a *wind bow shock*. The two bow shock cases are similar in that the external stream is oblivious to the presence of the star until it suddenly hits the bow shock shell, differing only in whether it is radiation or wind that is providing the internal pressure. In the intermediate bow wave case, on the other hand, the external stream is gradually decelerated by absorption of photons as it approaches the bow.⁷

We now consider the application to bow shocks around main sequence OB stars, expressing stellar and ambient parameters in terms of typical values as follows:

$$\begin{aligned} \dot{M}_{-7} &= \dot{M}/(10^{-7} M_\odot \text{ yr}^{-1}) \\ V_3 &= V/(1000 \text{ km s}^{-1}) \\ L_4 &= L/(10^4 L_\odot) \\ v_{10} &= v_\infty/(10 \text{ km s}^{-1}) \\ n &= (\rho/\bar{m})/(1 \text{ cm}^{-3}) \\ \kappa_{600} &= \kappa/(600 \text{ cm}^2 \text{ g}^{-1}), \end{aligned}$$

where \bar{m} is the mean mass per hydrogen nucleon ($\bar{m} \approx 1.3m_p \approx 2.17 \times 10^{-24} \text{ g}$ for solar abundances). Note that $\kappa = 600 \text{ cm}^2 \text{ g}^{-1}$ corresponds to a cross section of $\approx 10^{-21} \text{ cm}^2$ per hydrogen nucleon, which is typical for interstellar medium dust (Bertoldi & Draine 1996) at far ultraviolet wavelengths, where OB stars emit most of

⁶ We implicitly assume that the interaction of the stellar wind with the external stream can always be treated in the continuum limit. This will be true if either the collisional mean free path or the ion Larmor radius is much smaller than R_0 , which is almost always the case.

⁷ A shock does still form in this case, but shocked material constitutes only a fraction of the total column density of the shell, see § G.

their radiation. In terms of these parameters, we can express the stellar wind momentum efficiency as

$$\eta = 0.495 \dot{M}_{-7} V_3 L_4^{-1} \quad (12)$$

and the fiducial radius and optical depth as

$$R_*/\text{pc} = 2.21 (L_4/n)^{1/2} v_{10}^{-1} \quad (13)$$

$$\tau_* = 0.0089 \kappa_{600} (L_4 n)^{1/2} v_{10}^{-1}. \quad (14)$$

In Figure 2, we show results for the bow size (apex distance, R_0) as a function of the density, n , and relative velocity, v_∞ , of the external stream, with each panel corresponding to a particular star, with parameters as shown in Table 1. To facilitate comparison with previous work, we choose stellar parameters similar to those used in the hydrodynamical simulations of Meyer et al. (2014, 2016, 2017), based on stellar evolution tracks for stars of $10 M_\odot$, $20 M_\odot$ and $40 M_\odot$ (Brott et al. 2011) and theoretical wind prescriptions (de Jager et al. 1988; Vink et al. 2000). Although the stellar parameters do evolve with time, they change relatively little during the main-sequence lifetime of several million years.⁸ The three examples are an early B star ($10 M_\odot$), a late O star ($20 M_\odot$), and an early O star ($40 M_\odot$), which cover the range of luminosities and wind strengths expected from bow-producing hot main sequence stars. The luminosity is a steep function of stellar mass ($L \sim M^{2.5}$) and the wind mass-loss rate is a steep function of luminosity ($\dot{M} \sim L^{2.2}$), which means that the wind momentum efficiency is also a steep function of mass ($\eta \sim M^3$), approaching unity for early O stars, but falling to less than 1% for B stars.

It can be seen from Figure 2 that the onset of the radiation bow wave regime is very similar for the three main-sequence stars, occurring at $n > 20$ to $40 v_{10}^2$. An important difference, however, is that for the $40 M_\odot$ star, which has a powerful wind, the radiation bow wave regime only occurs for a very narrow range of densities, whereas for the $10 M_\odot$ star, with a much weaker wind, the regime is much broader, extending to $n < 10^4 v_{10}^2$. Another difference is the size scale of the bows in this regime, which is $R_0 = 0.001 \text{ pc}$ to 0.003 pc for the $10 M_\odot$ star if $v_\infty = 40 \text{ km s}^{-1}$, but $R_0 \approx 0.1 \text{ pc}$ for the $40 M_\odot$ star, assuming the same inflow velocity.

Figure 3 shows results for a cool M-type super-giant star with stellar parameters inspired by Betelgeuse (α Orionis), as listed in Table 1. Unlike the UV-dominated spectrum of the hot stars, this star emits predominantly in the near-infrared, where the dust extinction efficiency is lower, so we adopt a lower opacity of $60 \text{ cm}^2 \text{ g}^{-1}$. This has the effect of shifting the radiation bow wave regime to higher densities: $n = 1000$ to $30000 v_{10}^2$ in this case.

⁸ Note that we have recalculated the stellar wind terminal velocities, since the values given in the Meyer et al. papers are troublingly low. We have used the prescription $V = 2.6V_{\text{esc}}$, where $V_{\text{esc}} = (2GM(1 - \Gamma_e)/R)^{1/2}$ is the photospheric escape velocity, which is appropriate for strong line-driven winds with $T_{\text{eff}} > 21000 \text{ K}$ (Lamers et al. 1995). We find velocities of 2500 km s^{-1} to 3300 km s^{-1} , which are consistent with observations and theory (Vink et al. 1999) for O stars, but at least two times higher than those cited by Meyer et al. (2014). For main-sequence B stars, wind column densities are too low to reliably measure the terminal velocity from near ultraviolet P Cygni profiles (Prinja 1989), and so the values are theory-dependent (Krtička 2014) and hence more uncertain. A further complication is the existence of a subset of OB stars with anomalously weak winds (Puls et al. 2008), which in some cases is related to the presence of strong ($\sim 1 \text{ kG}$) magnetic fields (Oskinova et al. 2011).

Table 1. Stellar parameters for example stars

	M/M_{\odot}	L_4	\dot{M}_{-7}	V_3	η	Sp. Type	T_{eff}/kK	$\lambda_{\text{eff}}/\mu\text{m}$	S_{49}	Figures
Main-sequence OB stars	10	0.63	0.0034	2.47	0.0066	B1.5 V	25.2	0.115	0.00013	2a, 8, 9
	20	5.45	0.492	2.66	0.1199	O9 V	33.9	0.086	0.16	2b
	40	22.2	5.1	3.31	0.4468	O5 V	42.5	0.068	1.41	2c
Blue supergiant star	33	30.2	20.2	0.93	0.3079	B0.7 Ia	23.5	0.123	0.016	4
Red supergiant star	20	15.6	100	0.015	0.0476	M1 Ia	3.6	0.805	0	3

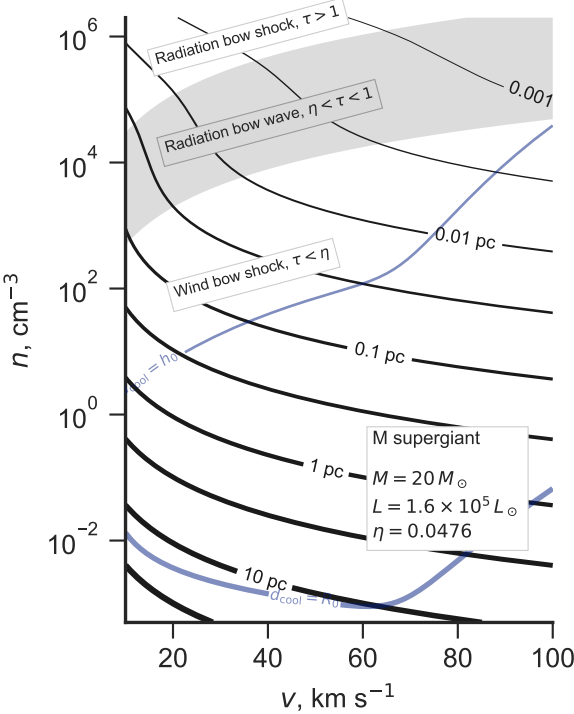


Figure 3. As Fig. 2, but for a cool M-type supergiant instead of hot main sequence stars. A smaller dust opacity is used, $\kappa = 60 \text{ cm}^2 \text{ g}^{-1}$, because of the reduced extinction efficiency at the optical/infrared wavelengths emitted by this star.

2.1.2 Effects of stellar gravity

In principle, gravitational attraction from the star, of mass M , will partially counteract the radiative acceleration. This can be accounted for by replacing L with an effective luminosity

$$L_{\text{eff}} = L(1 - \Gamma_{\text{E}}^{-1}), \quad (15)$$

in which Γ_{E} is the Eddington factor:

$$\Gamma_{\text{E}} = \frac{\kappa L}{4\pi c GM} = 458.5 \frac{\kappa_{600} L_4}{M}, \quad (16)$$

where, in the last expression, M is measured in solar masses. For the stars in Table 1, we find $\Gamma_{\text{E}} \approx 30$ to 400, so gravity can be safely ignored. The only exception is when the optical depth of the bow is very large: $\tau > \ln \Gamma_{\text{E}} \sim 5$, in which case gravity may be important in the outer parts of the shell (see Rodríguez-Ramírez & Raga 2016).

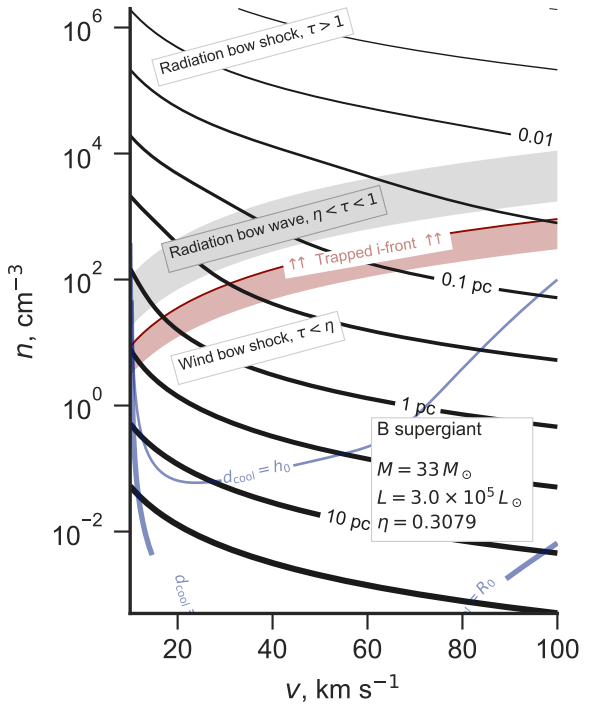


Figure 4. As Fig. 2, but for an evolved B-type supergiant instead of main sequence stars. This is similar to the early O MS star of Fig. 2c in many respects, except for the trapping of the ionization front, which occurs for much lower outer stream densities.

2.1.3 Ionization state of the bow shell

In this section we calculate whether the star is capable of photoionizing the entire bow shock shell, or whether the ionization front will be trapped within it. The number of hydrogen recombinations⁹ per unit time per unit area in a fully ionized shell is

$$\mathcal{R} = \alpha_B n_{\text{sh}}^2 h_{\text{sh}}, \quad (17)$$

while the advective flux of hydrogen nuclei through the shock is

$$\mathcal{A} = nv, \quad (18)$$

⁹ The diffuse field is treated in the on-the-spot approximation, assuming all emitted Lyman continuum photons are immediately re-absorbed locally, so the case B recombination co-efficient, $\alpha_B = 2.6 \times 10^{-13} T_4^{-0.7} \text{ cm}^3 \text{ s}^{-1}$, is used, where $T_4 = T/10^4 \text{ K}$.

6 Henney, Arthur, & Tarango Yong

and the flux of hydrogen-ionizing photons ($h\nu > 13.6 \text{ eV}$) incident on the inner edge of the shell is

$$\mathcal{F} = \frac{S}{4\pi R_0^2}, \quad (19)$$

where S is the ionizing photon luminosity of the star. Any shell with $\mathcal{R} + \mathcal{A} > \mathcal{F}$ cannot be entirely photoionized by the star, and so must have trapped the ionization front.

The ratio of advective particle flux to ionizing flux is, from equations (3), (18), (19),

$$\frac{\mathcal{A}}{\mathcal{F}} = 5.86 \times 10^{-5} \frac{x^2 L_4}{v_{10} S_{49}}, \quad (20)$$

which is nearly always small. For clarity of exposition, we therefore ignore \mathcal{A} in the following discussion, although it is included in quantitative calculations. The column density of the shocked shell can be found, for example, from equations (10) and (12) of Wilkin (1996) in the limit $v_\infty/V \rightarrow 0$ (Wilkin's parameter α) and $\theta \rightarrow 0$. This yields

$$n_{\text{sh}} h_{\text{sh}} = \frac{3}{4} n R_0. \quad (21)$$

Assuming strong cooling behind the shock,¹⁰ the shell density is

$$n_{\text{sh}} = M_0^2 n \quad (22)$$

where $M_0 = v_\infty/c_s$ is the isothermal Mach number of the external stream.¹¹ Putting these together with equations (3) and (9), one finds that $\mathcal{R} > \mathcal{F}$ implies

$$x^3 \tau_* > \frac{4Scc_s \bar{m}^2 \kappa}{3\alpha L}. \quad (23)$$

From equation (10), it can be seen that x depends on the external stream parameters, n, v_∞ only via τ_* , and so equation (23) is a condition for τ_* , which, by using equation (14), becomes a condition on n/v_{10}^2 . In the radiation bow shock case, $x = (1 + \eta)^{1/2}$, and the condition can be written:

$$\frac{n}{v_{10}^2} > 2.65 \times 10^8 \frac{S_{49}^2 T_4^{3.4}}{L_4^3 (1 + \eta)^3}, \quad (24)$$

where

$$S_{49} = S/(10^{49} \text{ s}^{-1}).$$

Numerical values of S_{49} for our three example stars are given in Table 1, taken from Figure 4 of Sternberg et al. (2003). In the radiation bow wave case, $x = 2\tau_*$, and the condition can be written:

$$\frac{n}{v_{10}^2} > 5.36 \times 10^4 \frac{S_{49}^{1/2} T_4^{0.85}}{\kappa_{600}^{3/2} L_4^{3/2}}. \quad (25)$$

In the wind bow shock case, the result is the same as equation (24), but changing the factor $(1 + \eta)^3$ to η^3 . For the example hot stars in Table 1, and assuming $\kappa_{600} = 1, T_4 = 0.8$, the resulting density threshold is $n > (1000 \text{ to } 5000) v_{10}^2$, depending only weakly on the stellar parameters, which is shown by the red lines in Figure 2. For the $10 M_\odot$ star, this is in the radiation bow wave regime, whereas

¹⁰ This is shown to be justified in § 2.1.4.

¹¹ The sound speed depends on the temperature and hydrogen and helium ionization fractions, y and y_{He} as $c_s^2 = (1 + y + z_{\text{He}}y_{\text{He}})(kT/\bar{m})$, where z_{He} is the helium nucleon abundance by number relative to hydrogen and $k = 1.3806503 \times 10^{-16} \text{ erg K}^{-1}$ is Boltzmann's constant. We assume $y = 1, y_{\text{He}} = 0.5, z_{\text{He}} = 0.09$, so that $c_s = 11.4 T_4^{1/2} \text{ km s}^{-1}$.

for the higher mass stars it is in the radiation bow shock regime. When the external stream is denser than this, then the outer parts of the shocked shell may be neutral instead of ionized, giving rise to a cometary compact H II region (Mac Low et al. 1991; Arthur & Hoare 2006). This is only necessarily true, however, when the star is isolated. If the star is in a cluster environment, then the contribution of other nearby massive stars to the ionizing radiation field must be considered.

Quite different results are obtained for a B-type supergiant star (see Tab. 1 and Fig. 4), which has a similar bolometric luminosity and wind strength to the $40 M_\odot$ main-sequence star, but a hundred times lower ionizing luminosity. This results in a far lower threshold for trapping the ionization front of $n > 40v_{10}^2$. The advective flux, \mathcal{A} , is relatively stronger for this star than for the main-sequence stars, but even for $v_{10} < 2$, where the effect is strongest, the change is only of order the width of the dark red line in Figure 4.

In principle, when the ionization front trapping occurs in the bow wave regime, then the curves for R_0 will be modified in the region above the red line because all of the ionizing radiation is trapped in the shell due to gas opacity, which is not included in equation (8). However, this only happens for our $10 M_\odot$ star, which has a relatively soft spectrum. Table 1 gives the peak wavelength of the stellar spectrum for this star as $\lambda_{\text{eff}} = 0.115 \mu\text{m}$, which is significantly larger than the hydrogen ionization threshold at $0.0912 \mu\text{m}$, meaning that only a small fraction of the total stellar luminosity is in the EUV band and affected by the gas opacity. The effect on R_0 is therefore small. For the higher mass stars, $\lambda_{\text{eff}} < 0.0912 \mu\text{m}$, so the majority of the luminosity is in the EUV band, but in these cases the ionization front trapping occurs well inside the radiation bow shock zone, where the dust optical depth is already sufficient to trap all of the radiative momentum.

2.1.4 Radiative cooling lengths

In this section, we calculate whether the radiative cooling is sufficiently rapid behind the bow shock to allow the formation of a thin, dense shell. Since cooling is least efficient at low densities, we will assume that the wind bow shock regime applies unless otherwise specified. We label quantities just outside the shock by the subscript “0”, quantities just inside the shock (after thermalization, but before any radiative cooling) by the subscript “1”, and quantities after the gas has cooled back to the photoionization equilibrium temperature by the subscript “2”. Assuming a ratio of specific heats, $\gamma = 5/3$, the relation between the pre-shock and immediate post-shock quantities is

$$\frac{n_1}{n_0} = \frac{4M_0^2}{M_0^2 + 3} \quad (26)$$

$$\frac{T_1}{T_0} = \frac{1}{16} (5M_0^2 - 1)(1 + 3/M_0^2) \quad (27)$$

$$\frac{v_1}{v_0} = \left(\frac{n_1}{n_0} \right)^{-1}, \quad (28)$$

where $M_0 = v_0/c_s$. The cooling length of the post-shock gas can be written as

$$d_{\text{cool}} = \frac{3P_1 v_1}{2(\mathcal{L}_1 - \mathcal{G}_1)}, \quad (29)$$

where P_1 is the thermal pressure and $\mathcal{L}_1, \mathcal{G}_1$ are the volumetric radiative cooling and heating rates. For fully photoionized gas, we have $P_1 \approx 2n_1 kT_1$, $\mathcal{L}_1 = n_1^2 \Lambda(T_1)$, and $\mathcal{G}_1 = n_1^2 \Gamma(T_1)$, where $\Lambda(T)$ is the cooling coefficient, which is dominated by metal emission

lines that are excited by electron collisions, and $\Gamma(T)$ is the heating coefficient, which is dominated by hydrogen photo-electrons (Osterbrock & Ferland 2006). The cooling coefficient has a maximum around 10⁵ K, and for typical ISM abundances can be approximated as follows:

$$\Lambda_{\text{warm}} = 3.3 \times 10^{-24} T_4^{2.3} \text{ erg cm}^{-3} \text{ s}^{-1} \quad (30)$$

$$\Lambda_{\text{hot}} = 10^{-20} T_4^{-1} \text{ erg cm}^{-3} \text{ s}^{-1} \quad (31)$$

$$\Lambda = \left(\Lambda_{\text{warm}}^{-k} + \Lambda_{\text{hot}}^{-k} \right)^{-1/k} \quad \text{with } k = 3, \quad (32)$$

which is valid in the range 0.7 < T_4 < 1000. We approximate the heating coefficient as

$$\Gamma = 1.77 \times 10^{-24} T_4^{-1/2} \text{ erg cm}^{-3} \text{ s}^{-1}, \quad (33)$$

where the coefficient is chosen so as to give $\Gamma = \Lambda$ at an equilibrium temperature of $T_4 = 0.8$.

In Figure 2 we show curves calculated from equations (26) to (33), corresponding to $d_{\text{cool}} = R_0$ (thick blue line) and $d_{\text{cool}} = h_0$ (thin blue line), where h_0 is the shell thickness in the efficient cooling case. In this context, $n_0 = n$ and $n_2 = n_{\text{sh}}$, so that h_0 follows from equations (21) and (22) as

$$h_0 = \frac{3}{4} M_0^{-2} R_0. \quad (34)$$

The bends in the curves at $v \approx 50 \text{ km s}^{-1}$ are due to the maximum in the cooling coefficient $\Lambda(T)$ around 10⁵ K. For bows with outer stream densities above the thin blue line, radiative cooling is so efficient that the bow shock can be considered isothermal, and so the shell is dense and thin (at least, in the apex region). It can be seen that the ionization front trapping always occurs at densities larger than this, which justifies the use of equation (22) in the previous section. For bows with outer stream densities below the thick blue line, cooling is unimportant and the bow shock can be considered non-radiative. In this case the shell is thicker than in the radiative case, $h_{\text{sh}}/R_0 \approx 0.2$ to 0.3.¹² For bows with outer stream densities between the two blue lines, cooling does occur, albeit inefficiently, so that the shell thickness is set by d_{cool} rather than h_0 .

2.2 Imperfect coupling between gas and dust

If the radiation field is sufficiently strong, then the collisional coupling between grains and gas will break down. In this section, we calculate the regions of star+stream parameter space where this might occur, leading to a separation of the bow into an outer dust wave and an inner, dust-free bow shock.

2.2.1 Drag force on grains

The drag force on a charged dust grain moving at a relative speed w through a plasma has contributions from both direct collisions and from electrostatic Coulomb interactions with ions and electrons. We use the expressions in Draine & Salpeter (1979), equations (4)–(6), considering the contributions from protons, electrons, helium

¹² An approximate value can be found from equation (21) by substituting $n = n_0$ and $n_{\text{sh}} \approx n_1$, then using equation (26). Consideration of the slight increase in density between the shock and the contact discontinuity reduces this value by 5–10%.

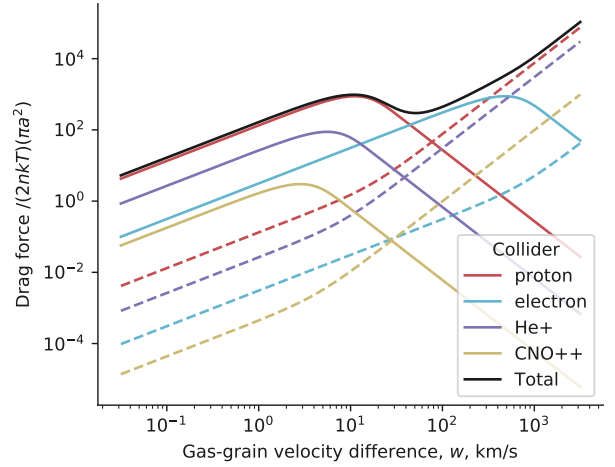


Figure 5. Contributions of different collider species to the dimensionless drag force, f_{drag}/f_* , as a function of gas–grain slip velocity, w . Solid lines show the Coulomb (electrostatic) drag, while dashed lines show the Epstein (solid-body) drag. Results are shown for dimensionless grain potential $\phi = 10$. All Coulomb forces scale with ϕ^2 , while the Epstein forces are independent of ϕ . The species labelled “CNO++” represents the combined effect of all metals (see footnote 14).

Table 2. Regimes of drag force as function of grain potential and slip speed

Regime	Approximate criteria	f_{drag}/f_*
I Epstein subsonic	$\phi^2 \ll 1$ and $w_{10} < 1$	$1.5 w_{10}$
II Epstein supersonic	$w_{10} > 1$ and $w_{10} > 5 \phi $	w_{10}^2
III Coulomb p ⁺ subthermal	$\phi^2 > 1$ and $w_{10} < 1$	$(1 + 20 \phi^2) w_{10}$
IV Coulomb p ⁺ superthermal	$\phi^2 > 1$ and $1 < w_{10} < 5$	$w_{10}^2 + 10 \phi^2 / w_{10}^2$
V Coulomb e ⁻ subthermal	$\phi^2 > 20$ and $5 < w_{10} < 42$	$0.48 \phi^2 w_{10}$

ions,¹³ and metal ions.¹⁴ Results are shown in Figure 5, where dashed lines correspond to direct solid body collisions and solid lines to electrostatic interactions. The latter depend on the grain potential, which is described in dimensionless terms by ϕ , which is the electrostatic potential energy of a unit charge at the surface of a grain of charge z_d and radius a , in units of the characteristic thermal energy of a gas particle:

$$\phi = \frac{e^2 z_d}{a k T}. \quad (35)$$

The electrostatic contributions to f_{drag} are proportional to ϕ^2 (results are shown for $|\phi| = 10$), whereas the solid-body contributions are independent of ϕ . The drag force is put in dimensionless units by

¹³ Helium is assumed to be singly ionized, leading to only a small contribution to the drag force. For much hotter stars, such as the central stars of planetary nebulae, helium may be doubly ionized, which leads to a fourfold increase in its Coulomb drag contribution, which is significant for $w < 5 \text{ km s}^{-1}$.

¹⁴ All metals are lumped together as a single species, assuming standard H II region gas-phase abundances. They are dominated by C and O, with minor contributions from N and Ne. The total abundance is 8.5×10^{-4} and the effective atomic weight is 15.3. All are assumed to be doubly ionized. Their largest relative contribution to the drag force is for $w < 2 \text{ km s}^{-1}$, but is less than 1% even there.

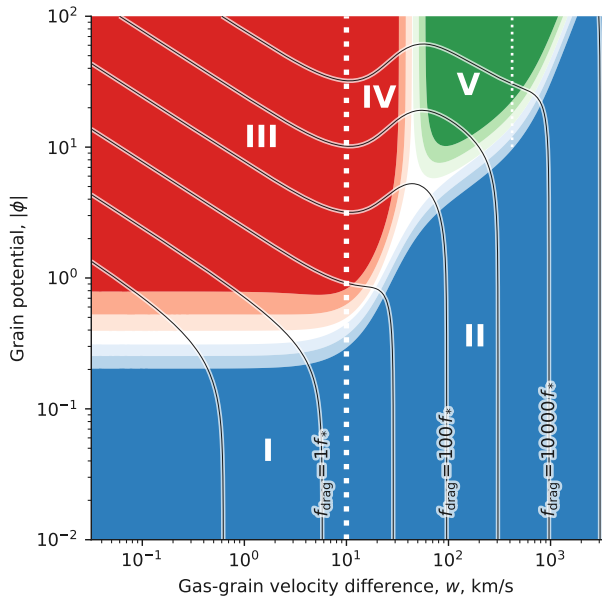


Figure 6. Regimes of gas–grain drag as a function of slip velocity and grain potential. The different regimes are indicated by bold roman numerals, as explained in Table 2. Blue shading indicates regions dominated by Epstein (solid-body) drag, whereas red and green shading indicate regions dominated by Coulomb drag due to protons and electrons, respectively. In each case, the saturated color represents a contribution > 70% of the relevant component to the total drag force, while progressively lighter shading represents the > 60% and > 50% levels. The thick white dotted line indicates the transition between the subthermal and superthermal regimes for protons, while the thin white dotted line indicates the corresponding transition for electrons. Contours show the total drag force in units of f_* (see eq. [36]) in decade intervals from 0.1 to 10^4 , as labelled. Results are shown for $T = 8000$ K and $n = 100 \text{ cm}^{-3}$, but the differences are very slight throughout the ranges $T = 5000$ K to $15\,000$ K and $n = 10^{-3} \text{ cm}^{-3}$ to 10^6 cm^{-3} .

dividing by a characteristic force:

$$f_* = 2nkT \cdot \pi a^2, \quad (36)$$

which is approximately¹⁵ the ionized gas pressure multiplied by the grain geometric cross section.

For grains with low electric charge, $\phi^2 \ll 1$, the drag force is dominated by direct collisions of protons with the grain (dashed red line in Fig. 5). The gas collisional mean free path is much larger than the grain size, so the drag is in the Epstein regime (Weidenschilling 1977). As the relative gas–grain slip speed, w , increases, f_{drag} first increases linearly with w reaching $f_{\text{drag}} \approx f_*$ at $w = c_s \approx 10 \text{ km s}^{-1}$, then transitions to a quadratic increase in the supersonic regime.

As $|\phi|$ increases, long-range electrostatic interactions with protons within the Debye radius (Coulomb drag) become increasingly important at subsonic relative velocities, as shown by the solid lines in Figure 5). However, the Coulomb drag has a peak when w is

¹⁵ To simplify the exposition, the gas pressure in this section is calculated assuming a fully ionized, pure hydrogen plasma, yielding $P_{\text{gas}} = 2nkT$. For typical ISM abundances, the contribution of helium and its corresponding electrons yield a correction to this of order 5%. The required modifications when a cool star interacts with a predominantly neutral gas stream are discussed later.

equal to the thermal speed of the colliders, which is $\approx 10 \text{ km s}^{-1}$ for protons, giving a maximum strength of

$$f_{\text{max}} = 0.5 (\ln \Lambda) \phi^2 f_* \approx 10 \phi^2 f_*, \quad (37)$$

where Λ is the plasma parameter (number of particles within a Debye volume), such that $\ln \Lambda = 23.267 + 1.5 \ln T_4 - 0.5 \ln n$. At highly super-thermal speeds, the Coulomb drag falls asymptotically as $f_{\text{drag}} \propto 1/w^2$. The thermal speed of electrons is higher than that of the protons by a factor of $(m_p/m_e)^{1/2}$, so that the electron Coulomb drag (solid light blue line) gives a second peak of similar strength, but at $w \approx 430 \text{ km s}^{-1}$. The behavior of f_{drag} in all these different regimes is summarised in Table 2, in terms of ϕ and $w_{10} = w/10 \text{ km s}^{-1}$. This is further illustrated in Figure 6, where each of the drag regimes is located on the $(w, |\phi|)$ plane.

2.2.2 Gas–grain separation: drift and rip

In Appendix B we calculate the behaviour of an incoming stream of dust grains, subject only to the repulsive radiation force from a star. For an initial inward radial trajectory, the dust grain motion is decelerated and turned around, reaching a minimum radius R_{**} , given by equation (B2). This drag-free radiative turnaround radius, R_{**} , is smaller for higher initial inward velocities, but is independent of the density of the incoming stream. We are now in a position to see how gas–grain drag will modify this picture.

From equations (B1) and (36), we can write the radiation force acting on a grain as

$$f_{\text{rad}} = Q_p \Xi f_*, \quad (38)$$

where Q_p is the grain’s radiation pressure efficiency (see footnote 20 in Appendix B) and Ξ is the local radiation parameter, defined as the ratio of direct stellar radiation pressure to gas pressure:

$$\Xi \equiv \frac{P_{\text{rad}}}{P_{\text{gas}}} \approx \frac{L}{4\pi R^2 c (2nKT)}, \quad (39)$$

where the last expression corresponds to the optically thin limit. The grain potential ϕ is also primarily determined by Ξ , as shown in Appendix A and the inset graph of Figure 7, but with a slow dependence, which can be approximated as

$$\phi(\Xi) \approx 1.5(2.3 + \ln \Xi). \quad (40)$$

There are also slight secondary dependencies on the grain composition and stellar spectrum. The relationship given in eq. (40) is appropriate for graphite grains and for stellar effective temperatures in the range 20 kK to 30 kK. For hotter stars than this, ϕ should be multiplied by a further factor of 1.5, while for silicate grains it should be divided by 1.5.

In the outer regions of the photoionized volume around an OB star, close to the ionization front, the radiation parameter is low, with typical value $\Xi \sim 0.1$. In this regime, the negative charge current at the grain surface due to electron collisions is roughly in balance with the positive current due to the ultraviolet photoelectric effect (Weingartner & Draine 2001), leading to a low grain potential, $|\phi| < 1$, which may be positive or negative. The low Ξ means that the radiative force is also weak: $f_{\text{rad}} \sim 0.1 f_*$ from equation (38) if $Q_p \sim 1$ at UV wavelengths, which is true for all but the smallest grains. Thus, from the equations for f_{drag} given in Table 2, the radiative force can be balanced by Epstein drag if $w_{10} \sim 0.1$, leading to a small equilibrium drift velocity, $w_{\text{drift}} < 1 \text{ km s}^{-1}$, of the grains with respect to the gas. This drift is much smaller than the inward stream velocities that we are considering ($v_\infty > 10 \text{ km s}^{-1}$), so the

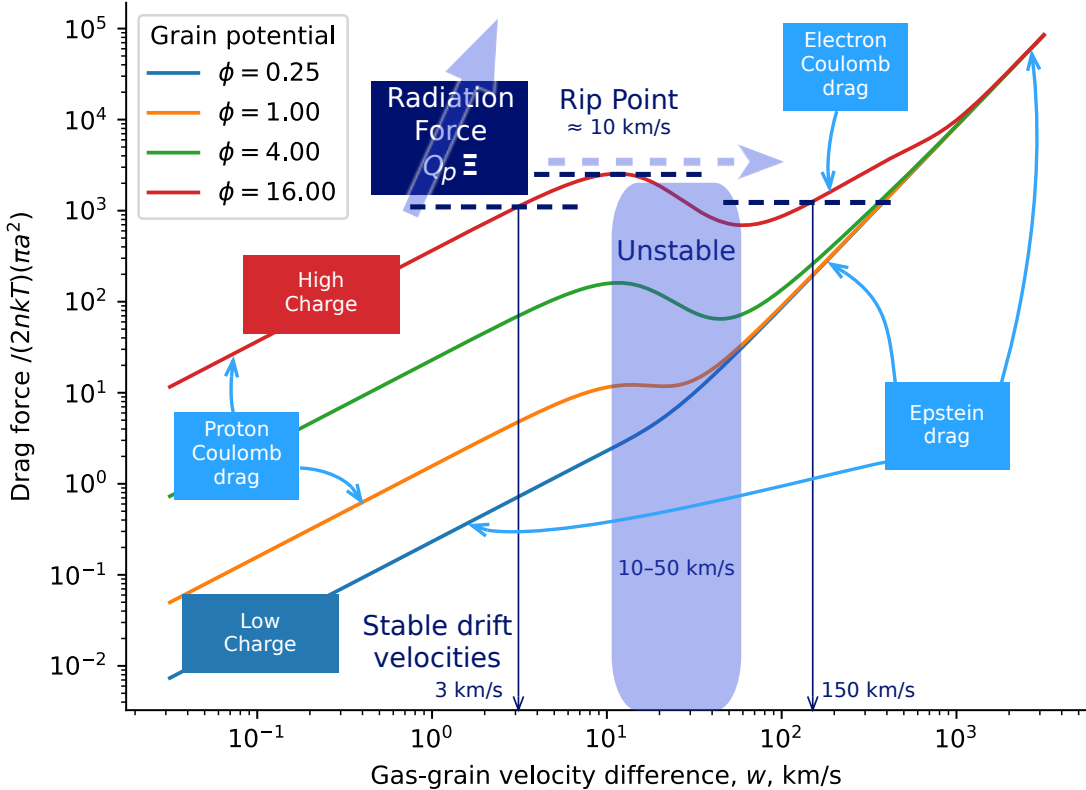


Figure 7. Dimensionless drag force, f_{drag}/f_e , as a function of gas–grain slip velocity, w , for different values of the grain potential in thermal units, ϕ . Contributions from proton and electron Coulomb (electrostatic) drag, as well as Epstein (solid-body) drag are indicated. Examples of subsonic and highly supersonic stable drift velocities are shown (thin dark blue arrows), where the drag force is in equilibrium with the radiation force (thick dark blue dashed lines), while blue shading indicates the unstable, mildly supersonic velocity regime, where no stable drift equilibrium exists. Inset graph shows ϕ as a function of the radiation parameter, $\Xi = P_{\text{rad}}/P_{\text{gas}}$ on a log–linear scale for a collection of Cloudy models (see Appendix A).

Table 3. Critical values of radiation parameter at the rip point: Ξ_{\dagger}

Spectrum	Grain composition	
	Graphite	Silicate
B star	1000 ± 400	350 ± 150
O star	3000 ± 500	2500 ± 500

Calculated from the Cloudy models shown in Figure A2. Uncertainties represent variations with grain size and gas density. See Appendix A for further details.

dust follows the gas stream at a slightly reduced velocity (< 10%), and (by mass conservation) a slightly increased density. Each grain exerts an exactly opposite force to f_{drag} upon the gas, but since the dust–gas mass ratio, Z_d , is small, this produces a negligible acceleration of the gas.

As the dusty stream approaches the star, the radiation parameter Ξ will increase, with a dependence of R^{-2} once the stream is well inside the ionization front. This increases f_{rad} (eq. [38]), but also increases the grain potential, ϕ (eq. [40]) due to the increasing dominance of grain charging by photoelectric ejection. Initially, this results in a lowering of the equilibrium drift velocity to $w_{10} \sim 0.01$ as the Coulomb drag kicks in (see Appendix A). However, at smaller

radii the slow logarithmic increase in $\phi(\Xi)$ means that the drift velocity must start increasing again to accommodate the linear increase of $f_{\text{rad}}(\Xi)$. Eventually, f_{rad} exceeds f_{max} , the maximum drag force that proton Coulomb interactions can provide (eq. [37]). This occurs at a critical value of the radiation parameter, which we denote the *rip point*: $\Xi_{\dagger} \sim 1000$. The variations in Ξ_{\dagger} with star and grain parameters, which are of order ± 0.5 dex, are listed in Table 3 and illustrated graphically in Figure A2.

2.2.3 Existence conditions for dust waves

In order for a separate dust wave to exist, it is necessary for the grains to decouple from the incoming gas stream before the stream hits the hydrodynamic bow shock caused by the stellar wind. The radius of the rip point, R_{\dagger} , can be expressed in terms of R_* , the fiducial optically thick bow shock radius introduced in § 2.1:

$$R_{\dagger} = \frac{v_{\infty}}{c_s} \Xi_{\dagger}^{-1/2} R_* \approx v_{10} \Xi_{\dagger}^{-1/2} R_*, \quad (41)$$

where we have made use of equations (3) and (39). The wind bow shock radius is $R_0 = \eta^{1/2} R_*$ (eq. [11]), where η is the wind momentum efficiency (eq. [12]). Therefore, the condition $R_{\dagger} > R_0$

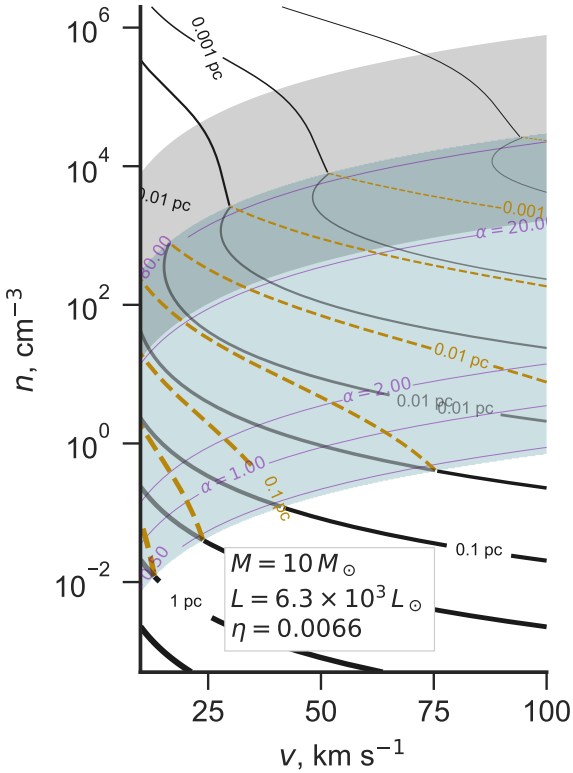


Figure 8. As Fig. 2(a), but accounting for gas-grain decoupling with constant efficiency $\xi = 0.07$.

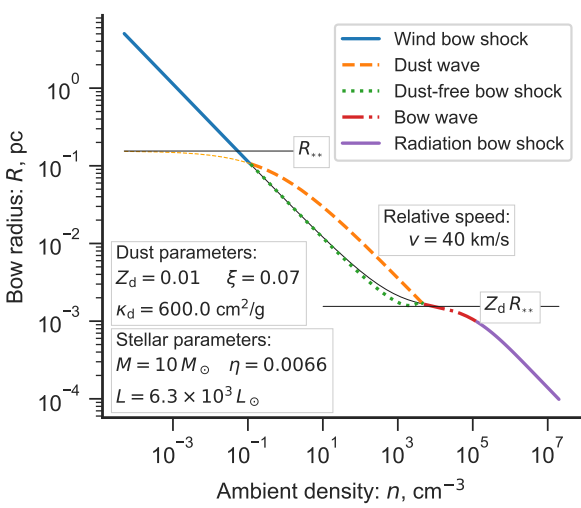


Figure 9. Vertical cut through Fig. 8, showing bow radius and different regimes for a fixed inflow velocity of 40 km s^{-1} .

becomes

$$v_{10} > v_{10,\min} = (\Xi_\dagger \eta)^{1/2}. \quad (42)$$

For O stars, the wind efficiency is generally high ($\eta > 0.1$) and $\Xi_\dagger > 2000$ (Tab. 3), so that dust waves can only exist when the stream velocity is very high ($v_\infty > 150 \text{ km s}^{-1}$). For B stars, in contrast, the wind can be much weaker ($\eta < 0.01$) and Ξ_\dagger is also smaller, so that dust waves are permitted by this criterion for much lower stream velocities: ($v_\infty > 30 \text{ km s}^{-1}$).

However, there are other conditions that need to be satisfied in order for the dust wave to exist. For instance, the drag-free turnaround radius must also be outside the bow shock: $R_{**} > R_0$, otherwise the radiation is incapable of repelling the grain opportunely, even once it has decoupled from the gas. From equations (3), (9), and (B2) we find

$$\frac{R_{**}}{R_*} = \frac{2\sigma_d Q_p \tau_*}{\kappa m_d}, \quad (43)$$

so, if we define a single-grain opacity as $\kappa_d = \sigma_d Q_p / m_d$, then this condition becomes

$$\tau_* > \tau_{*,\min} = 0.5 \frac{\kappa}{\kappa_d} \eta^{1/2}. \quad (44)$$

The average value of the factor κ/κ_d over the entire grain population must be equal to the dust–gas mass ratio, $Z_d \approx 0.01$, but the factor will vary between grains, according to their size and composition.¹⁶ In particular, it will be relatively larger for the largest grains ($a \approx 0.2 \mu\text{m}$), which dominate the total dust mass, and smaller for the smaller grains ($a \approx 0.02 \mu\text{m}$), which dominate the UV opacity. Given the dependence of τ_* on the stream parameters (eq. [14]), for a given stellar luminosity this condition corresponds to a minimum value for n/v_∞^2 .

A third condition comes from requiring $R_\dagger > R_0$ in the radiation bow wave regime (see § 2.1.1), where $R_0 \approx 2\tau_* R_*$. This yields

$$\tau_* < \tau_{*,\max} = 0.5 v_{10} \Xi_\dagger^{-1/2}, \quad (45)$$

which, for a given stellar luminosity, corresponds to a maximum value for n/v_∞^4 . Thus, for a given stream velocity that satisfies equation (42), equations (44, 45) determine respectively the minimum and maximum stream density for which a dust wave can exist.

Further restrictions on the existence of dust waves arise when the effects of magnetic fields are considered, as will be discussed in § 2.2.5 below.

2.2.4 Grain trajectories along the symmetry axis

What happens to the dust grain following this catastrophic breakdown of gas–grain coupling depends on the relation between the rip point radius, R_\dagger , and the drag-free radiative turnaround radius, R_{**} . If $R_\dagger > R_{**}$, then the grain’s inertia will still carry it in as far as R_{**} and the initial trajectory will be almost identical to that described in Appendix B for the drag-free case. However, after being turned around by the radiation field and pushed out past R_\dagger again, the grain will *recouple* to the gas and be dragged back for a second approach.¹⁷ From equations (41, 43, 45), the condition $R_\dagger > R_{**}$ corresponds

¹⁶ Remember that κ is the opacity per unit mass of gas, while κ_d is the opacity per unit mass of a particular grain. In both cases, averaged over the stellar spectrum.

¹⁷ If the initial impact parameter of the trajectory is not strictly $b = 0$, then the resultant lateral component of f_{rad} will mean that b will be much increased for the second approach.

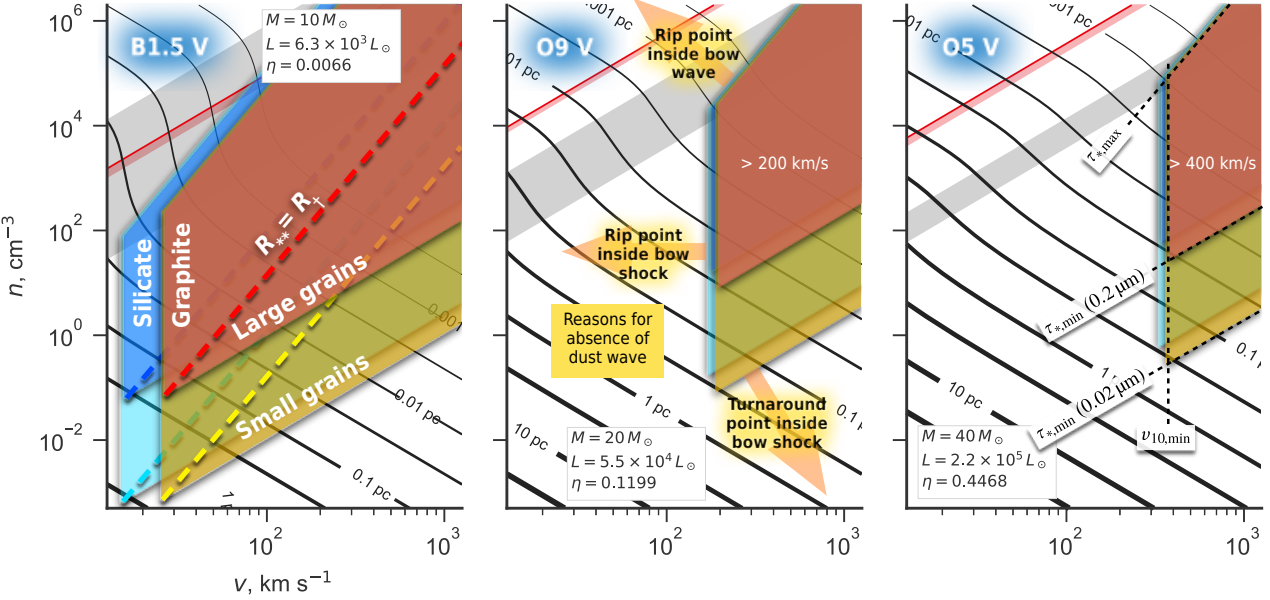


Figure 10. Regions of stream parameter space (v, n) where dust waves may form around main-sequence OB stars of $10 M_{\odot}$, $20 M_{\odot}$ and $40 M_{\odot}$ (see Tab. 1). Figure is similar to Fig. 2, except that the velocity axis is logarithmic and extends out to 1000 km s^{-1} . Overlapping colored shapes show parameters where dust waves may be allowed in the cases of large ($a = 0.2 \mu\text{m}$) and small ($a = 0.02 \mu\text{m}$) graphite and silicate grains, as labeled in the left panel. For (v, n) outside of these shapes, dust waves cannot occur for the reasons indicated by labeled orange arrows in the center panel. Labeled dashed lines in the right panel show the correspondence between the region boundaries and each dust wave existence condition given in equations (42, 44, 45). Heavy dashed lines in the left panel show where the rip point and the drag-free turnaround radius coincide. For dust waves below these lines, drag forces are unimportant for the grains.

to $\tau_* < (\kappa/\kappa_d)\tau_{*,\max}$, which is indicated by dashed lines in the left panel of Figure 10. If, on the other hand, $R_{\dagger} < R_{**}$, then the tail wind provided by the gas carries the grain closer to the star than its inertia would naturally take it. When the grain finally decouples at R_{\dagger} it experiences a much higher unbalanced f_{rad} , which can initially accelerate it to outward velocities significantly higher than the inflow velocity if $R_{\dagger} \ll R_{**}$.

The post-decoupling behavior of the grain depends on the sign of df_{drag}/dw when $w = |v_{\infty}|$. If this derivative is positive, as is the case in drag regimes II and V (see Tab. 2 and Fig. 6), then the grain can reach a stable equilibrium drift at rest with respect to the star¹⁸ at a point R_{\ddagger} , which we call the *stagnant drift radius*. If the stream velocity is not excessively high ($v_{\infty} < 150 \text{ km s}^{-1}$ when $\phi = 4$, or $< 300 \text{ km s}^{-1}$ when $\phi = 16$), then the equilibrium f_{rad} is less than the value at the rip point, requiring a lower value of the radiation parameter: $\Xi_{\ddagger} < \Xi_{\dagger}$. The resultant stagnant drift radius is therefore outside the rip point: $R_{\ddagger} > R_{\dagger}$.

whether or not the incoming stream velocity lies in drag regime IV (Table 2) with , which produces the unstable drift region identified in Figure 7.

2.2.5 Magnetic effects on grain trajectories

3 THE CASE OF INSIDE-OUT BOWS

So far, we have considered the case where the inner source dominates the radiation, while dust is present only in the outer stream, which applies to hot stars interacting with the ISM. However, in the case of cool stars, the inner wind will also be dusty. Examples are the red supergiant (RSG) phase of high-mass evolution, or the asymptotic giant branch (AGB) stage of low/intermediate-mass evolution. In both these cases, it is still the inner source that provides the radiation field. However, not all winds are radiatively driven and in those cases it is conceivable that it is the outer source that dominates the radiation field. An example is the case of photoevaporating protoplanetary disks (proplyds) in the Orion Nebula and other H II regions (O'Dell & Wen 1994). In the proplyds, the inner wind is a thermally driven photoevaporation flow (Henney & Arthur 1998; Henney & O'Dell 1999), while the outer stream is the stellar wind from an O star (García-Arredondo et al. 2001).

1

4 PERTURBED BOWS

The bow shock models that we have considered so far have been steady-state: although material is moving throughout the bow, the pattern of its structure does not vary with time. In this section, we consider small, time-varying perturbations to such a steady-state structure. These may be due to periodic variations in the momentum-loss rate of one of the winds, or due to dynamical instabilities in the shocked shell.

We consider fractional perturbations $\Delta(\theta, t)$ of a base shape

¹⁸ Again, this is only strictly true when the impact parameter is zero. However, as we show below, it is a reasonable approximation over a range of impact parameters in the case where the angle between the magnetic field direction and the stream velocity is not too large.

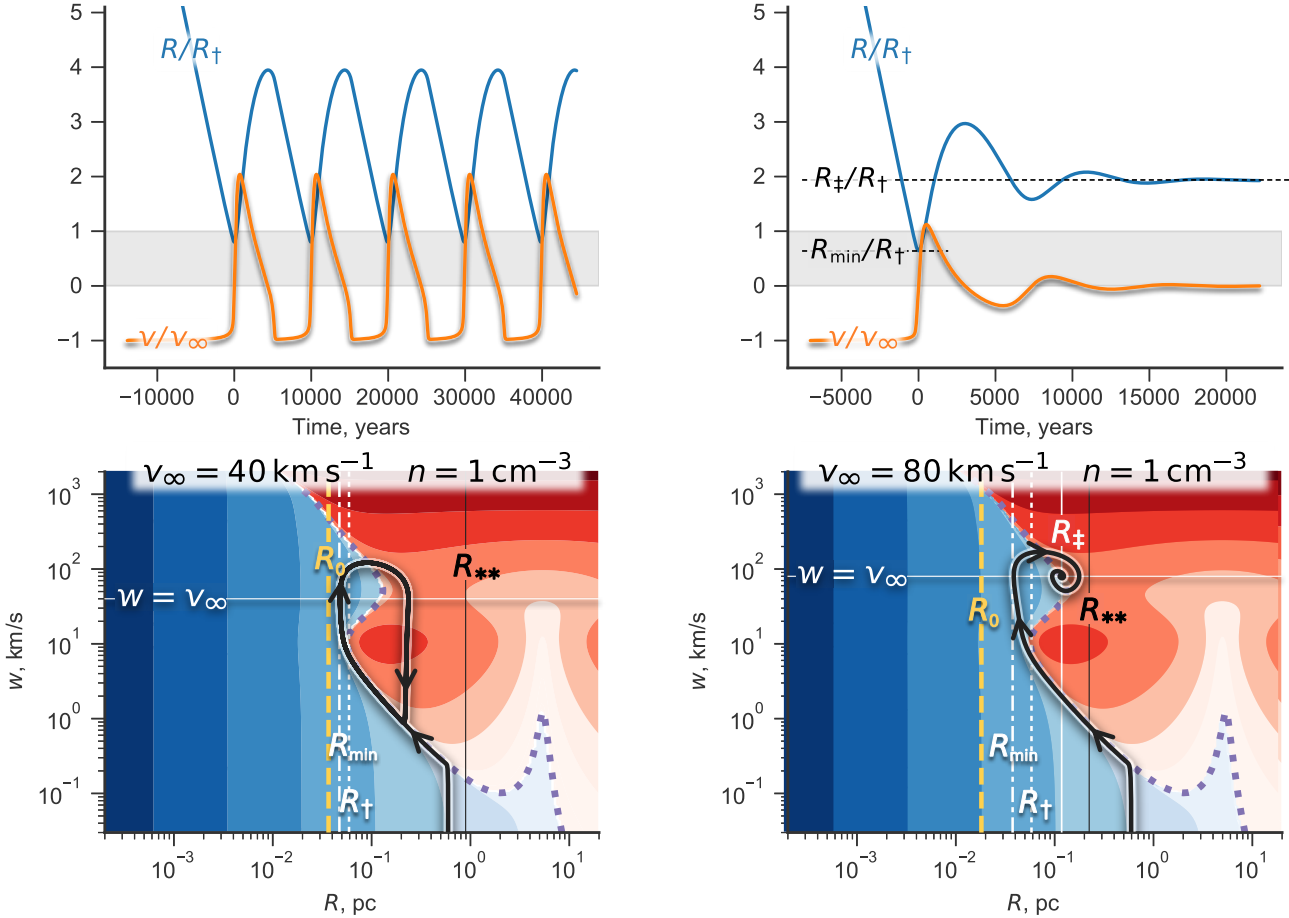


Figure 11. Phase space trajectories along the symmetry axis

$R(\theta)$, such that $R(\theta) \rightarrow [1 + \Delta(\theta, t)]R(\theta)$. For simplicity, $\Delta(\theta, t)$ is a standing wave of constant amplitude A , which is periodic in θ , with wave number N . In cylindrical symmetry $\Delta(\theta, t)$ must be even in θ , so can be expressed as

$$\Delta(\theta, t) = A \cos(N\theta) \cos(2\pi\varphi). \quad (46)$$

For waves with period P , the fractional phase φ will vary with time t as

$$\varphi(t) = (\varphi_0 + t/P) \bmod 1.0, \quad (47)$$

where φ_0 is an arbitrary reference phase.

Example oscillations with wave numbers $N = 1.0, 2.0$, and 5.0 superimposed on a wilkinoid base shape are shown in Figure 12. There are N nodes of the oscillation between $\theta = [0, \pi]$, always with an antinode at the apex ($\theta = 0$), as required by symmetry. So, with $N = 1.0$ there is a node (fixed point) in the near wing at $\theta = \pi/2$, but an antinode in the far wing at $\theta = \pi$, which is in antiphase with the oscillation of the apex, giving rise to a large-scale ‘breathing’ mode of oscillation. With $N = 2.0$, there are nodes at $\theta = \pi/4$ and $3\pi/4$, while the antiphase antinode has moved to the near wing at $\theta = \pi/2$. There is still an antinode in the far wing at $\theta = \pi$ but it is now in phase with the apex, giving rise to a ‘curling-up/straightening-out’ mode of oscillation. With $N = 5.0$, there are many more nodes and antinodes, giving a ‘ringing’ mode of oscillation. Note that all

our examples have $A \propto 1/N$ in order to keep the local curvature relatively low. If the product AN is not small compared to unity, then the local curvature can be so extreme as to reverse the concave shape of the base bow shape, producing locally convex regions.

If the bow shape is viewed at different inclinations, then the effect of the oscillations on the projected shape will vary. In particular, the apex-to-wing interval in body-frame angle changes from $\theta = [0, \pi/2]$ at $i = 0$ to $\theta = [\theta_0, \theta_{90}]$ for general i , see equations (18) and (21) of Paper I. The difference $\theta_{90} - \theta_0$ is always a declining function of $|i|$, so the oscillations of the tangent line become increasingly stretched out as the inclination increases. This effect can be seen in Figure 13, which shows an example of the variation in projected perturbed shape with inclination angle for 3 different phases, this time for an ancantoid base shape and the $N = 2.0$ perturbation shown in Figure 12b. The most marked changes with phase are seen for low inclinations, whereas the changes are smaller, although still noticeable, for $|i| \geq 45^\circ$. If AN exceeds about 0.5, then the local curvature of the perturbations is so extreme that multiple tangent lines exist at intermediate inclinations, which produces the appearance of additional incomplete bright arcs inside the main arc of the bow.

[t!]

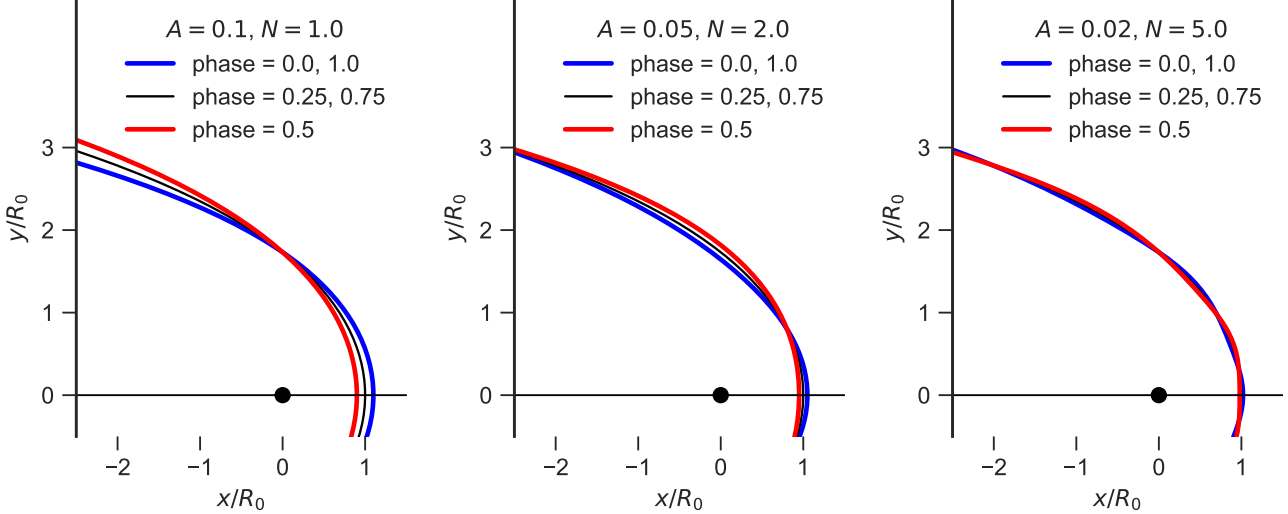


Figure 12. Small-amplitude standing wave perturbations to wilkinoid bow shapes. The maximum deviations from the base shape are seen at phases $\phi = 0$ (blue line) and $\phi = 0.5$ (red line), while the perturbation is zero at $\phi = 0.25$ and 0.75 (black line). Results are shown left to right for increasing wave numbers N and decreasing amplitudes A : (a) $A = 0.1$, $N = 1.0$, (b) $A = 0.05$, $N = 2.0$, (c) $A = 0.02$, $N = 5.0$.

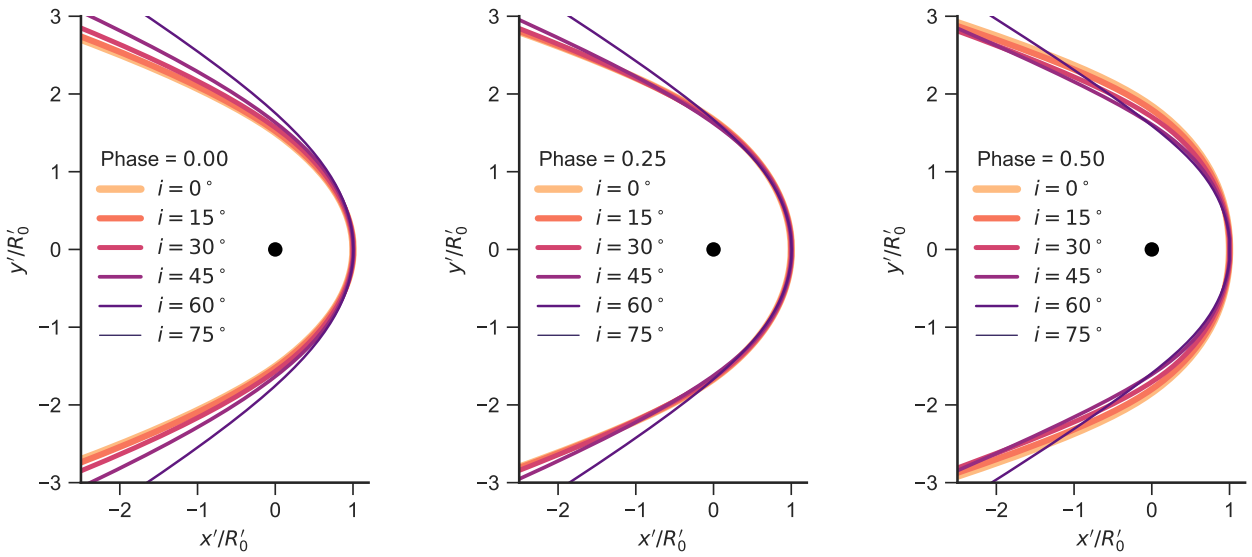


Figure 13. Plane-of-sky projections of perturbed bow shapes. In all cases, the base bow shape is ancantoid with $\xi = 0.8$, $\beta = 0.005$ and the perturbation is the same as in the central panel of Fig. 12, with amplitude $A = 0.05$ and wave number $N = 2.0$. Results are shown for inclination angles $i = 0$ to $i = 75^\circ$ (indicated by line color and thickness, see key) and for different fractional phases of the oscillation: (a) $\varphi = 0.0$, (b) $\varphi = 0.25$, (c) $\varphi = 0.50$. Unlike in Fig. 12, the spatial coordinates are normalized to the instantaneous projected apex radius R'_0 at each phase, so the apex does not appear to move.

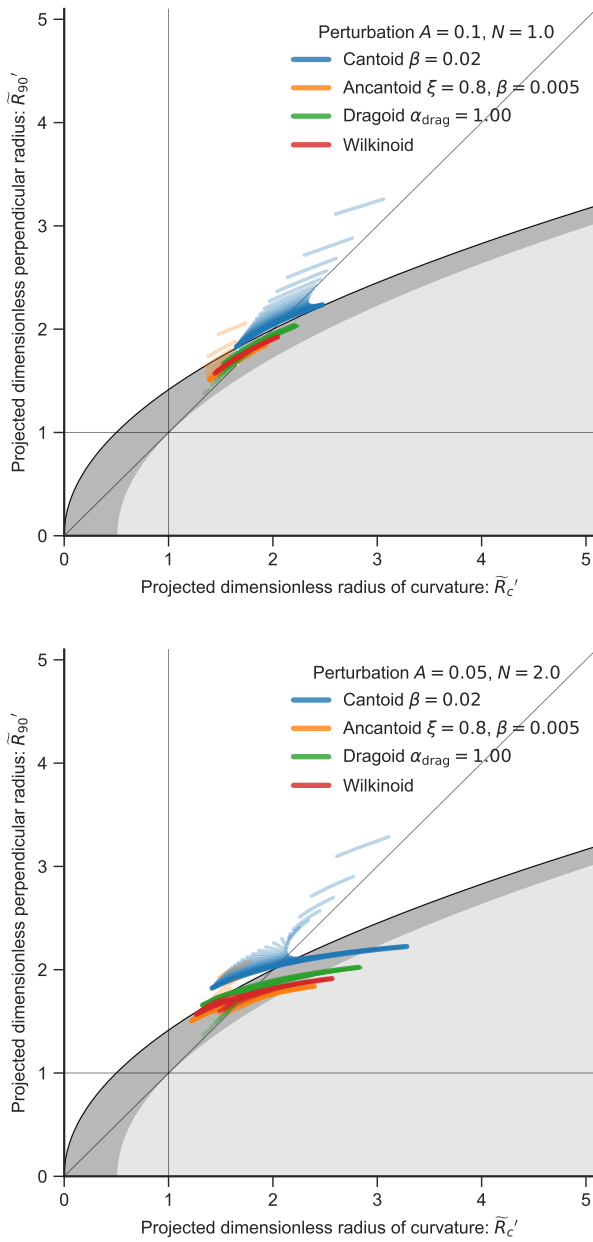


Figure 14. Diagnostic diagram for perturbed shapes

5 CASE STUDIES

Carina mid-infrared bow shocks (Sexton et al. 2015) are in a high density environment, 1000 cm^{-3} , so they may be bow waves. There seems to be spectral types for most of them: B0 (but supergiant) to O7. Sizes are 3 to 12 arcsec, which at Carina (2.3 kpc) is 0.033 pc to 0.134 pc.

Amazingly, the size/density combination gives regions that overlap with the dust wave region for both the $20 M_\odot$ and $40 M_\odot$ case. And implying velocities of 30 km s^{-1} to 50 km s^{-1} . This is more believable than the 10 km s^{-1} that they quote, since that would not give a shock at all. This would imply $\tau > \eta \approx 0.1$, so the bow luminosity should be 10% of the star luminosity, so getting on for $10^4 L_\odot$.

6 SUMMARY AND DISCUSSION

How different regions of the $\Pi-\Lambda$ plane are populated. Bottom-right quadrant hard to get to (except for standing wave oscillations), but may be due to finite shell thickness, which (for low Mach number) will be more apparent in the wings, which might decrease Λ more than Π . Fact that thin-shell solutions should trace the contact discontinuity, but in some cases it may be only the inner or the outer shell that is visible.

Justification for standing waves: Fig. 3 of Meyer et al. (2016) shows a time sequence of thin-shell instability, which looks a bit like a standing wave. But much larger amplitude than we are considering.

Deviations from axisymmetry as an alternative to oscillations.

REFERENCES

- Arthur S. J., Hoare M. G., 2006, ApJS, 165, 283
- Bertoldi F., Draine B. T., 1996, ApJ, 458, 222
- Bohren C. F., Huffman D., 1983, Absorption and scattering of light by small particles. Wiley-VCH
- Brott I., et al., 2011, A&A, 530, A115
- Canto J., Raga A. C., Wilkin F. P., 1996, ApJ, 469, 729
- Draine B. T., Salpeter E. E., 1979, ApJ, 231, 77
- García-Arredondo F., Henney W. J., Arthur S. J., 2001, ApJ, 561, 830
- Gull T. R., Sofia S., 1979, ApJ, 230, 782
- Henney W. J., Arthur S. J., 1998, AJ, 116, 322
- Henney W. J., O'Dell C. R., 1999, AJ, 118, 2350
- Henney W. J., Arthur S. J., Williams R. J. R., Ferland G. J., 2005, ApJ, 621, 328
- Hindmarsh A. C., 1983, IMACS Transactions on Scientific Computation, 1, 55
- Jones E., Oliphant T., Peterson P., et al., 2001–2018, SciPy: Open source scientific tools for Python, <http://www.scipy.org/>
- Krtička J., 2014, A&A, 564, A70
- Lamers H. J. G. L. M., Cassinelli J. P., 1999, Introduction to Stellar Winds. Cambridge, UK: Cambridge University Press
- Lamers H. J. G. L. M., Snow T. P., Lindholm D. M., 1995, ApJ, 455, 269
- Landau L., Lifshitz E., 1976, Mechanics, 3rd edn. Course of Theoretical Physics S Vol. 1, Butterworth-Heinemann
- Mac Low M.-M., van Buren D., Wood D. O. S., Churchwell E., 1991, ApJ, 369, 395
- Meyer D. M.-A., Mackey J., Langer N., Gvaramadze V. V., Mignone A., Izzard R. G., Kaper L., 2014, MNRAS, 444, 2754
- Meyer D. M.-A., van Marle A.-J., Kuiper R., Kley W., 2016, MNRAS, 459, 1146
- Meyer D. M.-A., Mignone A., Kuiper R., Raga A. C., Kley W., 2017, MNRAS, 464, 3229
- O'Dell C. R., Wen Z., 1994, ApJ, 436, 194
- Ochsendorf B. B., Tielens A. G. G. M., 2015, A&A, 576, A2
- Ochsendorf B. B., Cox N. L. J., Krijt S., Salgado F., Berné O., Bernard J. P., Kaper L., Tielens A. G. G. M., 2014a, A&A, 563, A65
- Ochsendorf B. B., Verdolini S., Cox N. L. J., Berné O., Kaper L., Tielens A. G. G. M., 2014b, A&A, 566, A75
- Osokinova L. M., Todt H., Ignace R., Brown J. C., Cassinelli J. P., Hamann W.-R., 2011, MNRAS, 416, 1456
- Osterbrock D. E., Ferland G. J., 2006, Astrophysics of gaseous nebulae and active galactic nuclei, second edn. Sausalito, CA: University Science Books
- Prinja R. K., 1989, MNRAS, 241, 721
- Puls J., Vink J. S., Najarro F., 2008, A&ARv, 16, 209
- Rodríguez-Ramírez J. C., Raga A. C., 2016, MNRAS, 460, 1876
- Sexton R. O., Povich M. S., Smith N., Babler B. L., Meade M. R., Rudolph A. L., 2015, MNRAS, 446, 1047
- Spitzer L., 1978, Physical processes in the interstellar medium. New York: Wiley-Interscience
- Sternberg A., Hoffmann T. L., Pauldrach A. W. A., 2003, ApJ, 599, 1333

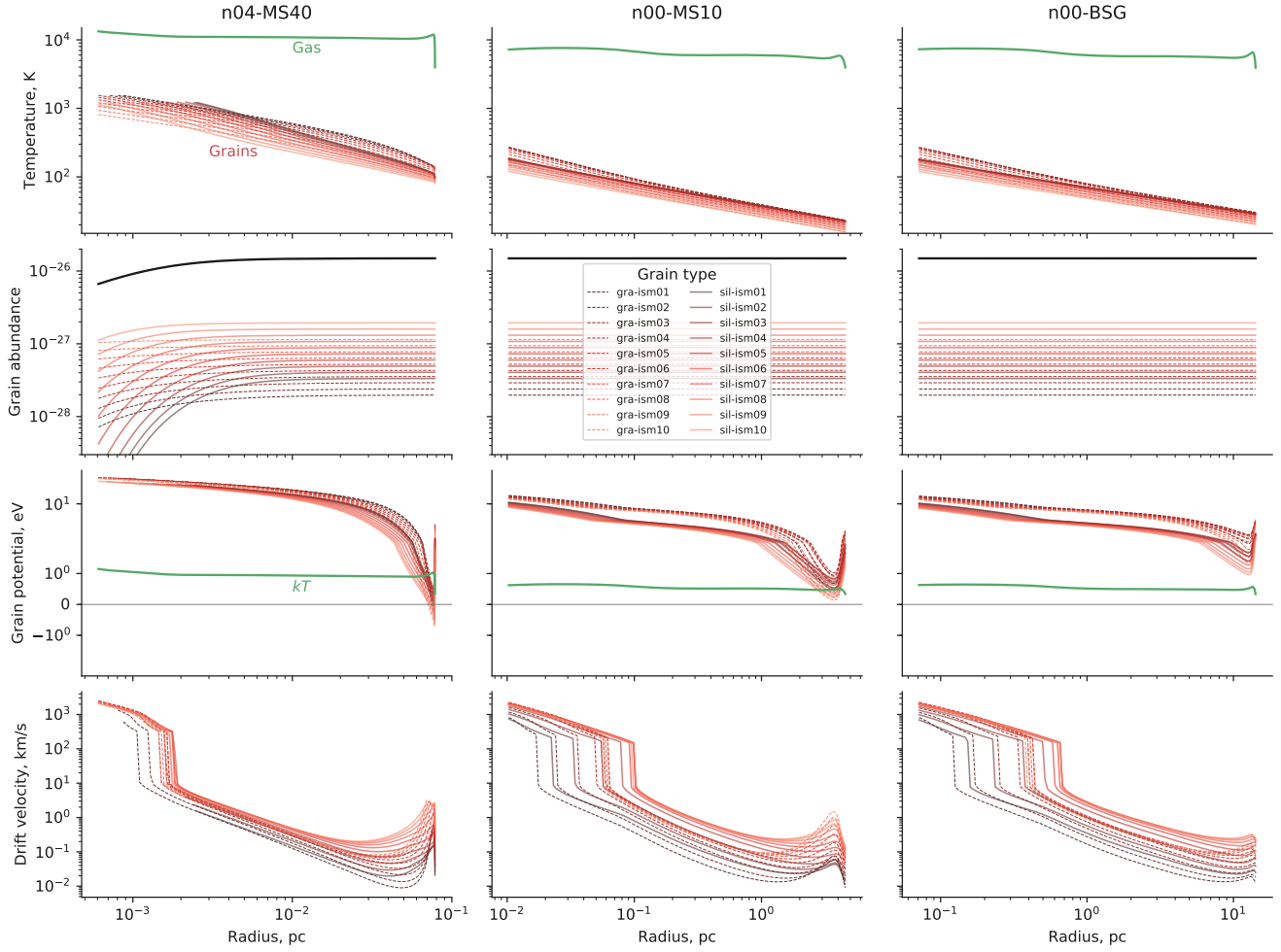


Figure A1. Dust properties as a function of radius from star for three selected Cloudy models. (a) $40 M_{\odot}$ main-sequence star in medium of density 10^4 cm^{-2} . (b) $10 M_{\odot}$ main-sequence star in medium of density 1 cm^{-2} . (c) Blue supergiant star in medium of density 1 cm^{-2}

Any deviation of w from w_{drift} produces unbalanced forces that tend to restore $w \rightarrow w_{\text{drift}}$, although the grain inertia means that this will not happen instantaneously, so that if w_{drift} varies rapidly along a streamline, then changes in w will lag behind. We define a dimensionless coupling coefficient, α_{drag} , to be the speed of the incoming stream in units of the drift velocity at the radiative turn-around radius:

$$\alpha_{\text{drag}} \equiv \frac{v_{\infty}}{w_{\text{drift}}(R_{**})} = \left(Q_{\text{drag}} \frac{R_{**}/a_{\text{d}}}{\rho_{\text{d}}/\rho_{\text{gas}}} \right)^{1/2}, \quad (\text{C3})$$

where we have used equation (B2) and suppressed a grain-shape dependent geometric factor of order unity. If $\alpha_{\text{drag}} \ll 1$, then $w_{\text{drift}} \gg v_{\infty}$ out to several times the turn-around radius, so the radiation field has no difficulty in effectively decoupling the grain from the gas and producing the velocity difference that is required to turn the grain around and expel it towards the direction whence it came ($w = 2v_{\infty}$). However, for non-zero α_{drag} the R^{-1} dependence of w_{drift} (eq. (C2)) means that the grain will *re-couple* to the inflowing gas stream around a radius $\approx R_{**}/\alpha_{\text{drag}}$ and be swept back in again for another approach to the source. A further effect of increasing α_{drag} is that the grain penetrates closer to the star on its initial approach, thanks to the tail wind provided by the gas flow. Both these behaviors

are illustrated in Figure B2, where the inertial lag of w behind w_{drift} means that the phase space trajectory (panel b) is a spiral, which converges on the stagnation point $(R, v) = (R_{**}/\alpha_{\text{drag}}, 0)$. The cases $\alpha_{\text{drag}} = 0.5$ and $\alpha_{\text{drag}} = 2$ are shown, and it can be seen that with larger α_{drag} the oscillations about the stagnation radius are significantly damped.

However, this description only applies to grains with impact parameter, b , that is exactly zero. Even a very small finite b means that f_{rad} has a component perpendicular to the axis, which pushes the grain to the side and means that, after re-coupling, its second approach is at a much larger impact parameter than its first, so it is dragged around the wings of the bow wave before it can bounce in and out more than twice. This is illustrated in Figure B3, which shows grain trajectories and the resulting dust density structure, calculated from numerical integration of equations (B1) and (C1) in 2-D cylindrical coordinates. Results are shown for a range of coupling parameters, α_{drag} . The $\alpha_{\text{drag}} = 0.25$ case appears qualitatively similar to the no-drag case shown in Figure B1a, except that the inner edge of the bow wave has been shifted to a smaller radius. Recoupling of the outgoing streamlines to the gas flow does occur eventually, but on length scales larger than shown in the figure. The $\alpha_{\text{drag}} = 0.5$ case

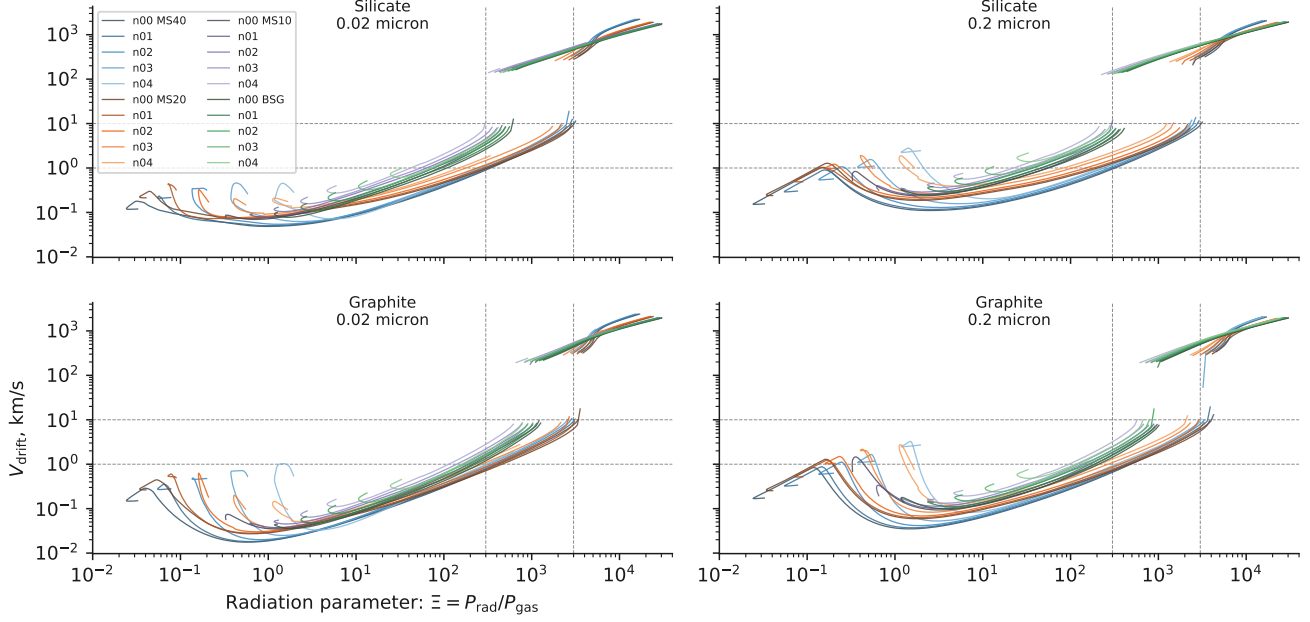


Figure A2. Drift velocity versus radiation parameter Ξ_P . Each line represents a model with ambient density and stellar type as indicated in the key.

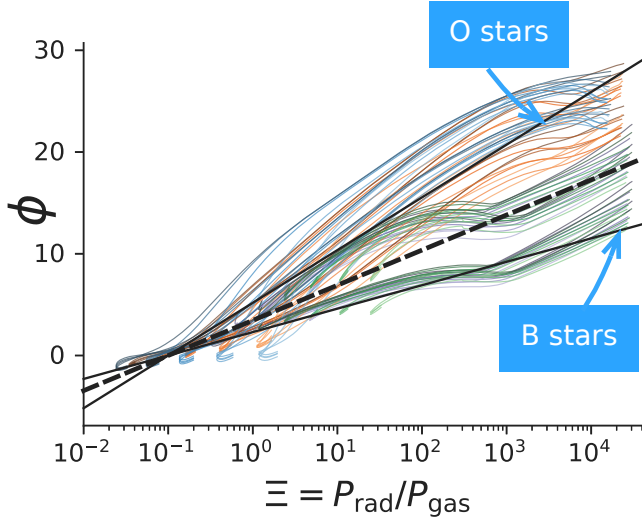


Figure A3. Grain potential versus radiation parameter

shows the oscillating trajectories discussed above for those grains that come in with a small initial impact parameter. In the $\alpha_{\text{drag}} = 1.0$ case, the oscillating trajectories are more confined, forming a thick shell around R_{**} . In the $\alpha_{\text{drag}} = 2.0$ case, the shell is much thinner and concentrated at the inner rim. As α_{drag} increases, the oscillations are damped further so that the stagnation radius $R_{**}/\alpha_{\text{drag}}$ becomes a good approximation to the apex radius of the density wave. All the cases illustrated are for a parallel incident stream, but a divergent stream gives qualitatively similar behavior, as shown in Appendix H. We propose the term *dragoid* for the 3-dimensional shapes of the bow waves, found by rotating results such as Figure B3 about the symmetry axis.

APPENDIX D: DUST WAVE WITH MAGNETIC FIELD

First consider the limit of very small gyro-radius, which is the case when the Lorentz force is much larger than other forces acting on the grain. The grains will then follow tightly wound helical paths around the magnetic field lines, which can be decomposed into a circular motion of radius r_L plus the motion of the *guiding center* along the field line. The motion of the guiding center is explicitly followed by accounting for the components parallel to the field lines of the radiative and drag forces, whereas forces perpendicular to the field lines, which would only effect the circular motion are ignored in the first instance (but see § XXX below).

D1 Resolved Larmor radius

APPENDIX E: APPLICABILITY OF THE DUST WAVE MODELS

The apex turn-around radius, R_{**} , of the bow wave depends on the grain properties via the combination $\sigma_d Q_p/m_d$. For grains of size a_d and internal density ρ_d , we have $\sigma_d/m_d \approx (a_d \rho_d)^{-1}$. For radiation with wavelength smaller than the grain size, $\lambda < a_d$, the efficiency is $Q_p \sim 1$, whereas for $\lambda > a_d$ it is $Q_p \sim a_d/\lambda$. Therefore, we would expect R_{**} to be almost independent of grain size for small grains, but to vary as $R_{**} \propto a_d^{-1}$ for large grains, where small/large is relative to the peak wavelength of the radiation source. In principle, a polydisperse population of grains could produce a blurring of the observed bow wave, but only if large grains contribute significantly to the dust emission.

Variation of α_{drag} with grain size, charged grains.

Lorentz force, Larmor radius

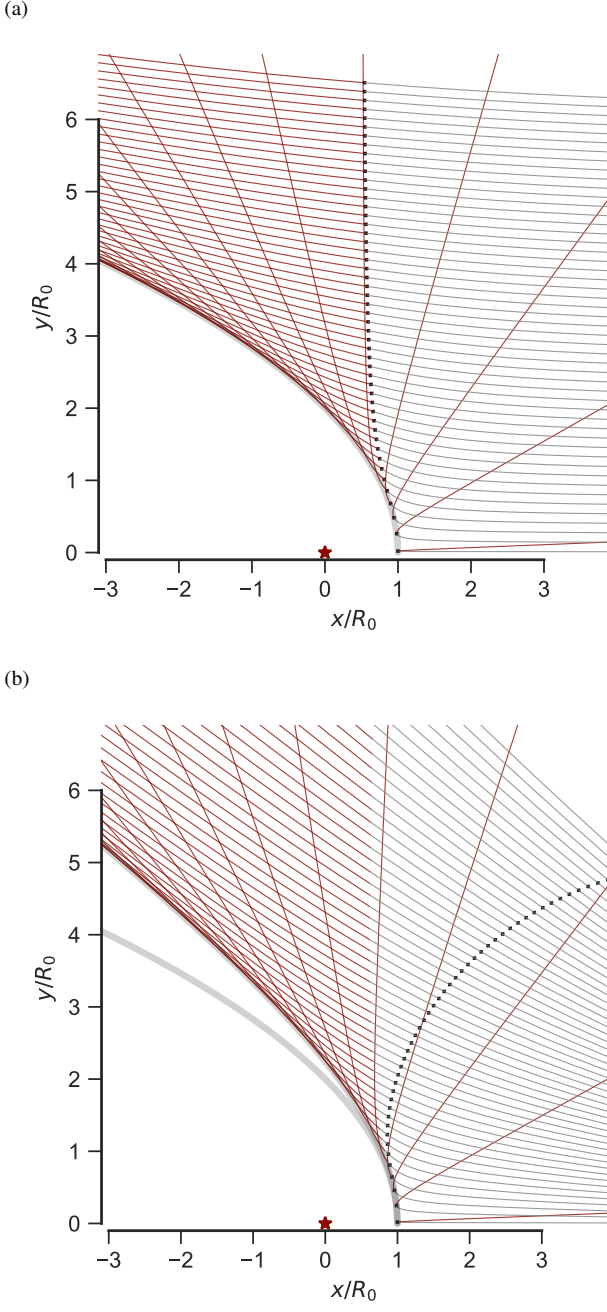


Figure B1. Dust grain trajectories under influence of a repulsive central r^{-2} radiative force. (a) A parallel stream of dust grains approach from the right at a uniform velocity and with a variety of impact parameters (initial y -coordinate). The central source is marked by a red star at the origin, and its radiative force deflects the trajectories into a hyperbolic shape, each of which reaches a minimum radius marked by a small black square. The incoming hyperbolic trajectories are traced in gray and the outgoing trajectories are traced in red. The locus of closest approach of the outgoing trajectories is parabolic in shape (traced by the thick, light gray line) and this constitutes the inner edge of the bow wave. (b) The same but for a divergent stream of dust grains that originates from a source on the x axis at a distance $D = 10R_{**}$ from the origin. In this case, the inner edge of the bow wave is hyperbolic and the parallel stream result is also shown for comparison.

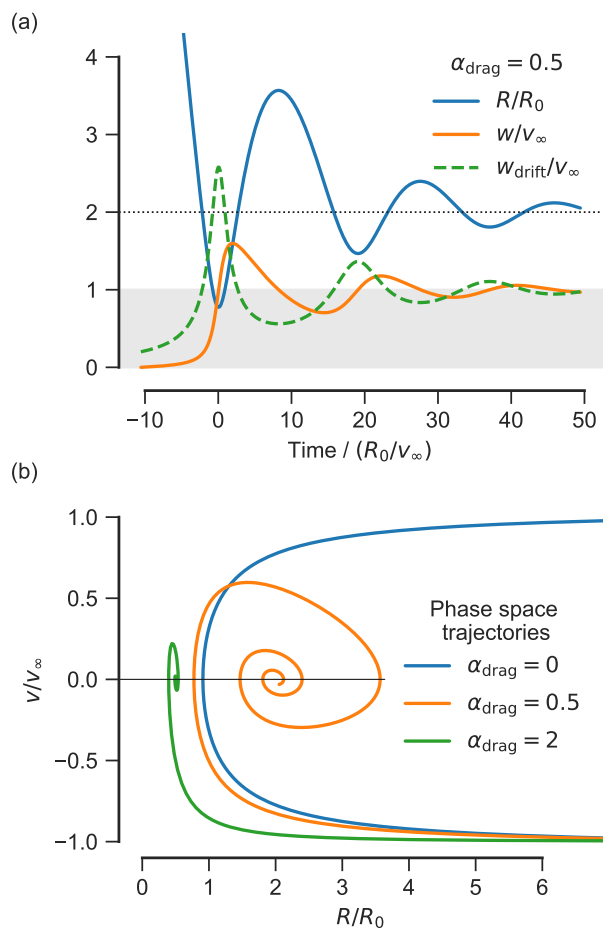


Figure B2. Dust-gas coupling for an on-axis (purely radial) trajectory. (a) Grain radial position, R/R_{**} , gas-grain velocity difference, w/v_∞ , and local asymptotic drift velocity, $w_{\text{drift}}/v_\infty$, versus time for $\alpha_{\text{drag}} = 0.5$. The behavior is typical of the dynamics of a damped harmonic oscillator. (b) Phase space (position, velocity) trajectories for $\alpha_{\text{drag}} = 0, 0.5$, and 2. All trajectories begin in the lower right corner and evolve in a clockwise direction. For $\alpha_{\text{drag}} > 0$, the grain spirals in on the point $(x, u) = (\alpha_{\text{drag}}^{-1}, 0)$.

Back-reaction on gas, $\alpha_{\text{drag}} \rightarrow \infty$, recovery of drag-free result for R_0 but with increased effective grain mass.

APPENDIX F: APPARENT SHAPES OF PROJECTED DRAGODIDS

APPENDIX G: SHAPE AND STRUCTURE OF BOW WAVES

APPENDIX H: EQUATIONS OF MOTION FOR GRAINS WITH RADIATION AND GAS DRAG

To find the dust grain trajectories $R_d(\theta)$ in the presence of radiation and drag forces (§ C), we numerically integrate the equations of motion. We define dimensionless cylindrical polar coordinates,

$$(X, Y) = \left(\frac{R_d(\theta) \cos \theta}{R_0}, \frac{R_d(\theta) \sin \theta}{R_0} \right), \quad (\text{H1})$$

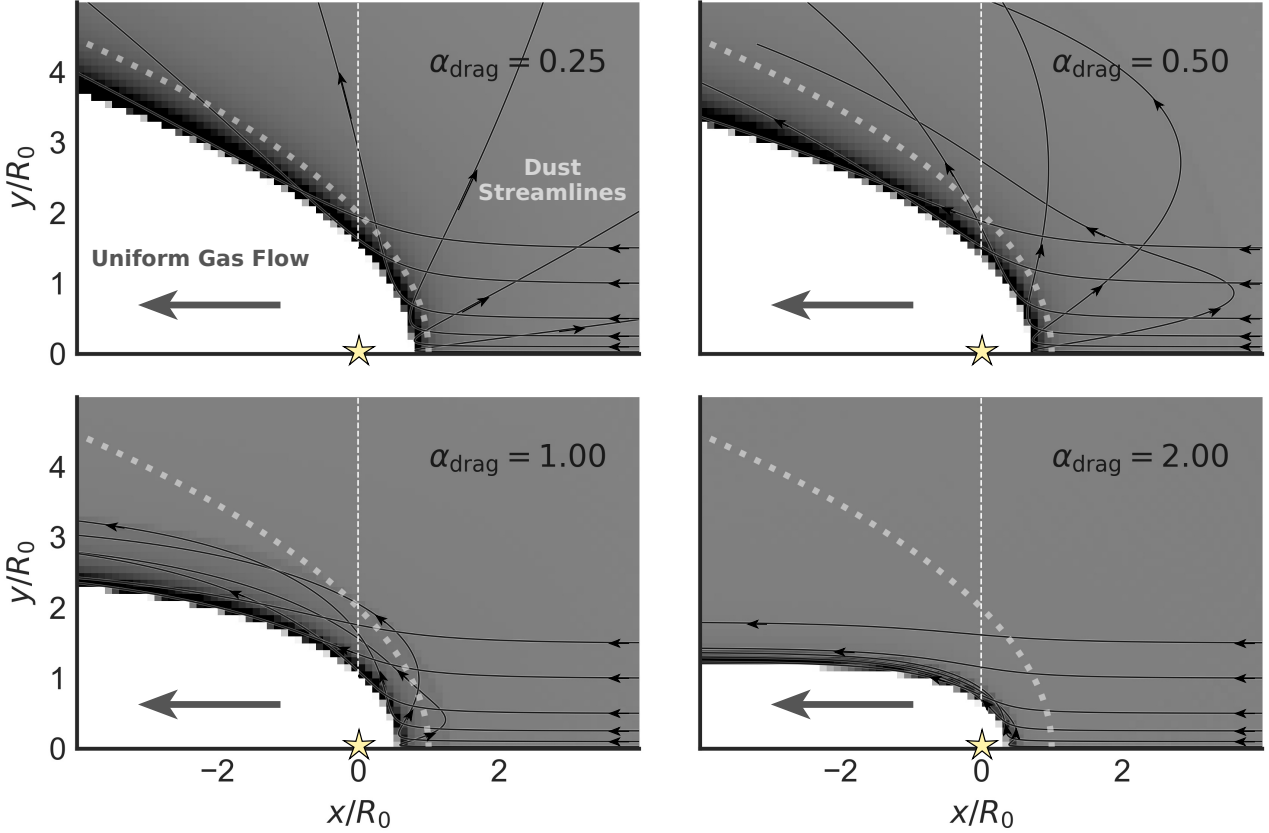


Figure B3. Dust grain trajectories under influence of gas drag in addition to a repulsive central radiative force. The dust streamlines are shown as black lines with arrows and the dust density as a linear gray scale, with maximum (black) of twice the ambient dust density. Results are shown for four values of the drag parameter (see text): $\alpha_{\text{drag}} = 0.25, 0.5, 1.0, \text{ and } 2.0$. The shape of the bow wave for the drag-free case (Fig. B1) is shown by the thick dotted line. Faint patterns visible in the density away from the bow wave are numerical aliasing artefacts caused by sparse sampling of the streamlines in the low density regions.

and dust grain velocities,

$$(U, V) = \left(\frac{\mathbf{v}_d \cdot \hat{\mathbf{x}}}{v_\infty}, \frac{\mathbf{v}_d \cdot \hat{\mathbf{y}}}{v_\infty} \right), \quad (\text{H2})$$

where $\hat{\mathbf{x}}$ and $\hat{\mathbf{y}}$ are unit vectors along the X and Y axes (parallel and perpendicular, respectively, to the symmetry axis). The grain equation of motion then follows from equations (B1, B2, C1–C3) as the following set of coupled differential equations:

$$\begin{aligned} \frac{dX}{dt} &= U & \frac{dY}{dt} &= V \\ \frac{dU}{dt} &= \frac{1}{2} \left[X \left(X^2 + Y^2 \right)^{-3/2} - \alpha_{\text{drag}}^2 D_1 (U - U_1) \right] \\ \frac{dV}{dt} &= \frac{1}{2} \left[Y \left(X^2 + Y^2 \right)^{-3/2} - \alpha_{\text{drag}}^2 D_1 (V - V_1) \right], \end{aligned} \quad (\text{H3})$$

where (U_1, V_1) are the components of the gas velocity (assumed fixed), given by

$$(U_1, V_1) = \begin{cases} \text{parallel stream} & (-1, 0) \\ \text{divergent stream} & \left(\frac{X - \mu^{-1}}{R_1}, \frac{Y}{R_1} \right), \end{cases} \quad (\text{H4})$$

where

$$R_1 = \left((X - \mu^{-1})^2 + Y^2 \right)^{1/2} \quad (\text{H5})$$

is the distance from the second source, located at $(X, Y) = (\mu^{-1}, 0)$. The dimensionless gas density, D_1 , normalized by the value at $(X, Y) = (1, 0)$, is

$$D_1 = \begin{cases} \text{parallel stream} & 1 \\ \text{divergent stream} & \frac{(\mu^{-1} - 1)^2}{R_1^2}. \end{cases} \quad (\text{H6})$$

Equations (H3) are integrated using the python wrapper `scipy.integrate.odeint` to the Fortran ODEPACK library (Hindmarsh 1983; Jones et al. 2018), with results shown in Figure B3 for parallel-stream cases and Figure H1 for divergent-stream cases.

APPENDIX I: FURTHER DETAILS ON IONIZATION FRONT TRAPPING

This appendix will probably be dropped from the paper. It contains details of the derivation of the ionization front trapping that I now think are too verbose to be included, given that this is not the main point of the paper. They are collected here for completeness.

We wish to calculate whether the star is capable of photoionizing the entire bow shock shell, or whether the ionization front will be

trapped within it. The number of hydrogen recombinations²² per unit time per unit area in a fully ionized shell is

$$\mathcal{R} = \alpha_B n_{\text{sh}}^2 h_{\text{sh}}, \quad (\text{I1})$$

while the flux of hydrogen-ionizing photons ($h\nu > 13.6 \text{ eV}$) incident on the inner edge of the shell is

$$\mathcal{F} = \frac{S}{4\pi R_0^2}, \quad (\text{I2})$$

where S is the ionizing photon luminosity of the star. Any shell with $\mathcal{R} > \mathcal{F}$ cannot be entirely photoionized by the star, and so must have trapped the ionization front. The column density of the shocked shell can be found, for example, from equations (10) and (12) of Wilkin (1996) in the limit $v_\infty/V \rightarrow 0$ (Wilkin's parameter α) and $\theta \rightarrow 0$. This yields

$$n_{\text{sh}} h_{\text{sh}} = \frac{3}{4} n R_0. \quad (\text{I3})$$

Assuming strong cooling behind the shock,²³ the shell density is $n_{\text{sh}} = M_0^2 n$, where $M_0 = v_\infty/c_s$ is the isothermal Mach number of the external stream.²⁴ Putting these together with equations (3) and (9), one finds that $\mathcal{R} > \mathcal{F}$ implies

$$x^3 \tau_* > \frac{4 S c_s \bar{m}^2 \kappa}{3 \alpha L}. \quad (\text{I4})$$

From equation (10), it can be seen that x depends on the external stream parameters, n, v_∞ only via τ_* , and so equation (23) is a condition for τ_* . In the radiation bow shock case, $x = (1 + \eta)^{1/2}$, and the condition can be written:

$$\tau_* > 145.0 \frac{S_{49} T_4^{1.7} \kappa_{600}}{L_4 (1 + \eta)^{3/2}}, \quad (\text{I5})$$

where

$$S_{49} = S / (10^{49} \text{ s}^{-1}).$$

Numerical values of S_{49} for our three example stars are given in Table 1. In the radiation bow wave case, $x = 2\tau_*$, and the condition can be written:

$$\tau_* > \left(18.1 \frac{S_{49} T_4^{1.7} \kappa_{600}}{L_4} \right)^{1/4}, \quad (\text{I6})$$

$\tau_* \sim n^{1/2}/v_\infty$ This simple criterion is shown by the dark red line in Figure 2. If $n/v_{10}^2 > 1000$ to 5000, depending only weakly on the stellar parameters, then the outer parts of the shocked shell are neutral, instead of ionized.

Assuming photoionization equilibrium, the hydrogen photoabsorption optical depth of the shell is

$$\tau_{\text{gas}} = -\ln(1 - \mathcal{R}/\mathcal{F}), \quad (\text{I7})$$

so long as $\mathcal{R} < \mathcal{F}$.

²² The diffuse field is treated in the on-the-spot approximation, assuming all emitted Lyman continuum photons are immediately re-absorbed locally, so the case B recombination co-efficient, $\alpha_B = 2.6 \times 10^{-13} T_4^{-0.7} \text{ cm}^3 \text{ s}^{-1}$, is used, where $T_4 = T/10^4 \text{ K}$.

²³ This is shown to be justified in § 2.1.4.

²⁴ The sound speed depends on the temperature and hydrogen and helium ionization fractions, y and y_{He} as $c_s^2 = (1 + y + z_{\text{He}}y_{\text{He}})(kT/\bar{m})$, where z_{He} is the helium nucleon abundance by number relative to hydrogen and $k = 1.380\,650\,3 \times 10^{-16} \text{ erg K}^{-1}$ is Boltzmann's constant. We assume $y = 1$, $y_{\text{He}} = 0.5$, $z_{\text{He}} = 0.09$, so that $c_s = 11.4 T_4^{1/2} \text{ km s}^{-1}$.

We will assume a typical photoionized temperature of 8000 K, so that $c_s \approx 10 \text{ km s}^{-1}$ and $M_0 = v_{10}$, yielding

$$\tau_{\text{gas}} = -\ln(1 - 8.42 \times 10^{-6} v_{10}^2 n^2 R_{0,\text{pc}}^3 S_{49}^{-1}), \quad (\text{I8})$$

where

$$R_{0,\text{pc}} = R_0 / (1 \text{ pc})$$

The dust opacity is approximately constant at FUV to EUV wavelengths, so the dust optical depth of the shocked shell to ionizing photons follows from equations (8) and (21) as $\tau_d = \frac{3}{8} \tau$.

The hydrogen ionization fraction, y , at the outer edge of the shocked shell then follows as

$$\frac{y^2}{1 - y} = \frac{\sigma \mathcal{F}}{\alpha_B n} e^{-(\tau_d + \tau_{\text{gas}})}, \quad (\text{I9})$$

where σ is the effective hydrogen photoionization cross section, averaged over the local ionizing spectrum. Since the frequency-dependent cross section, $\sigma_\nu \sim \nu^{-3}$, is strongly peaked at the threshold, the local EUV spectrum becomes harder with increasing τ_{gas} , as the lower frequency photons are selectively absorbed,²⁵ leading to a reduction in the effective σ . An approximate fit to the results in Appendix A of Henney et al. (2005) is

$$\sigma = 0.5 \sigma_0 e^{-\tau_{\text{gas}}/3} \quad (\text{I10})$$

where $\sigma_0 = 6 \times 10^{-18} \text{ cm}^2$ is the threshold cross-section. Although this was derived for a particular ionizing spectrum (40 000 K black body), we adopt it for all our hot stars.

This paper has been typeset from a TeX/LaTeX file prepared by the author.

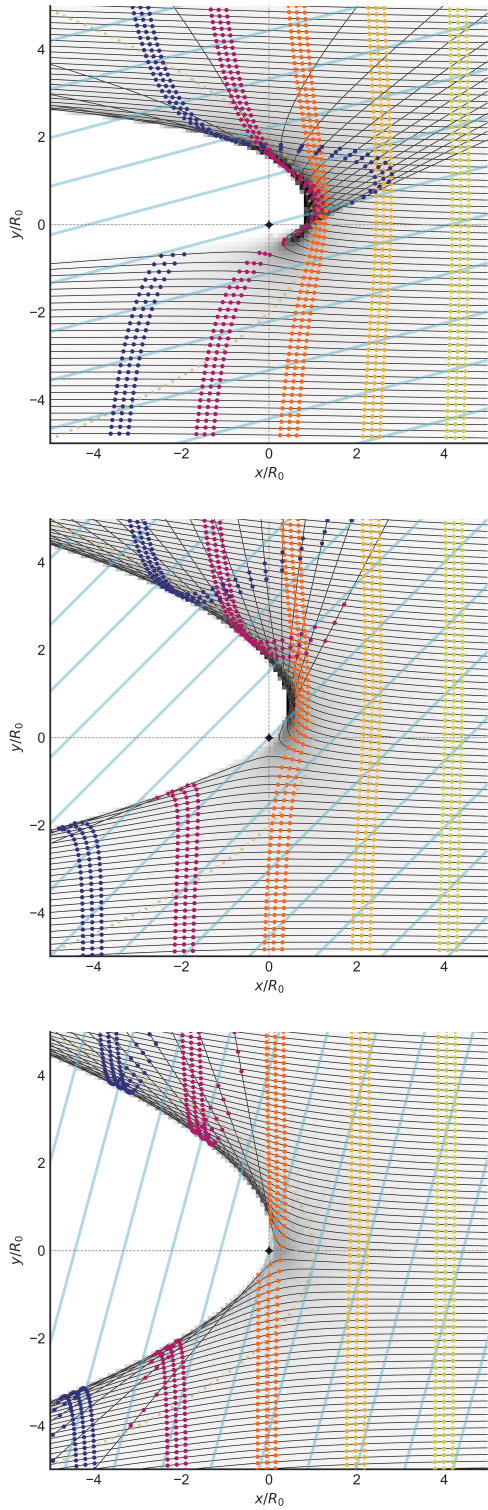
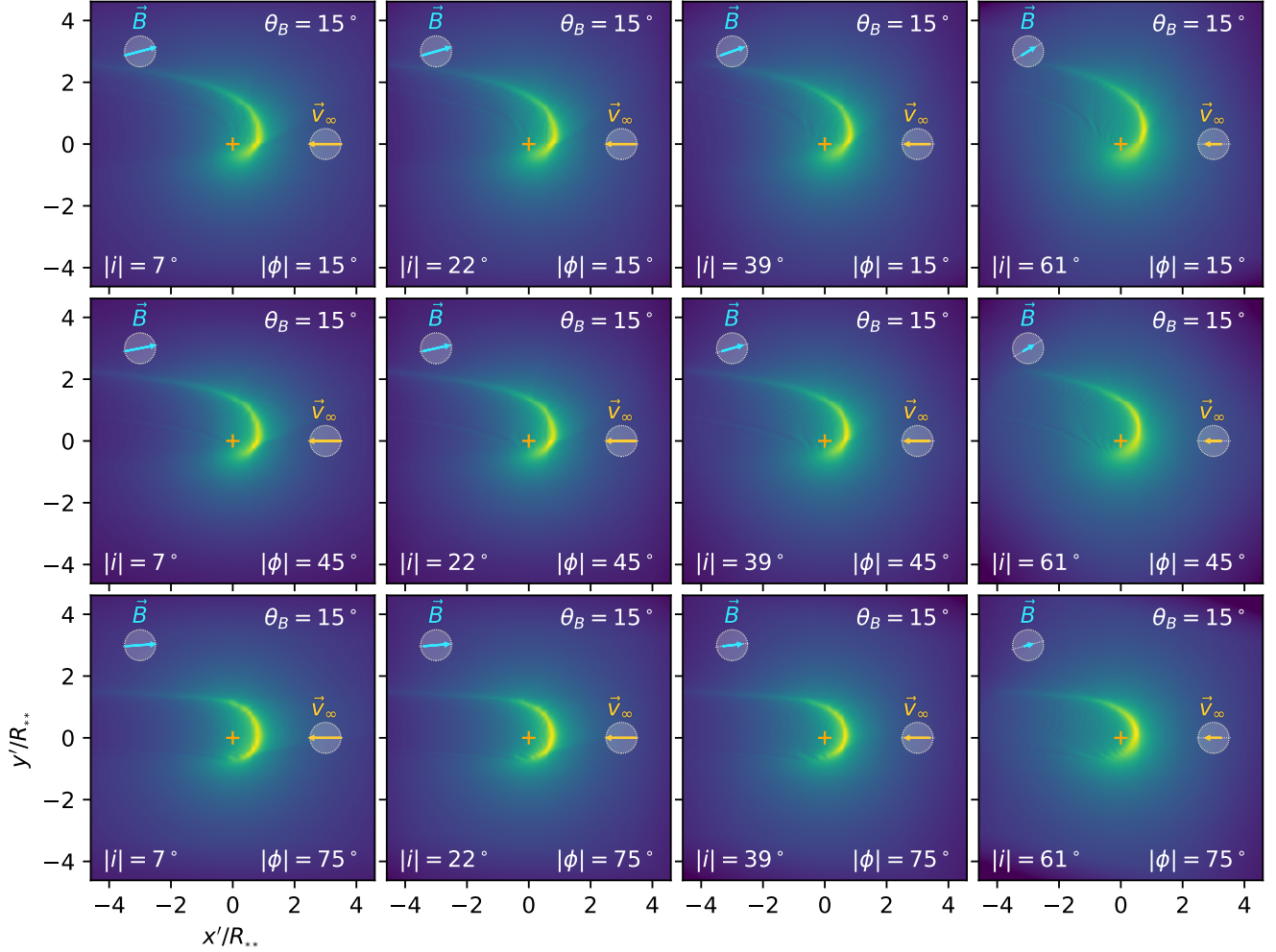


Figure D1. Grain trajectories for magnetised dust waves in the limit of no gas drag and small gyro-radius.

**Figure D2.** xxx

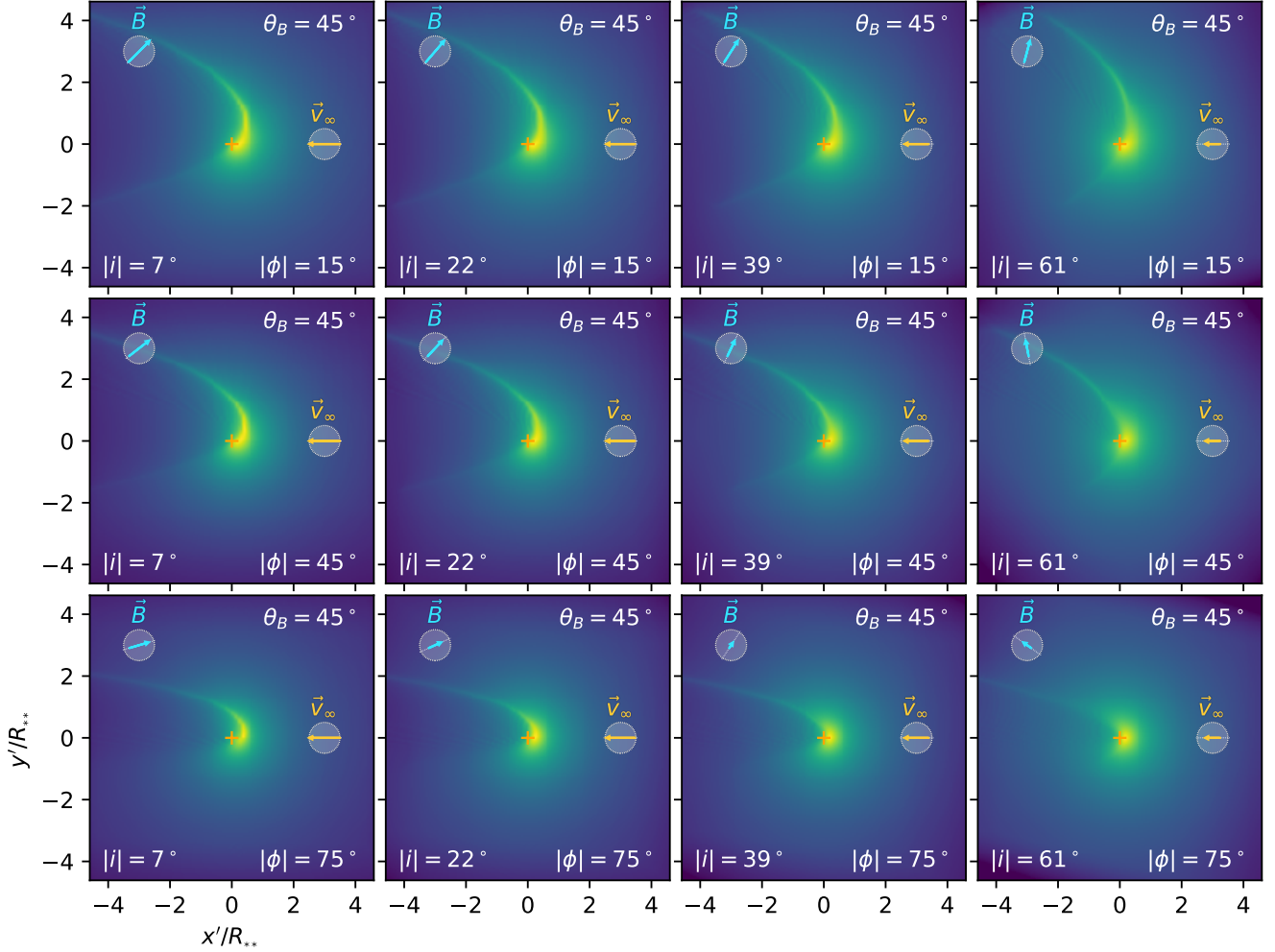


Figure D3. xxx

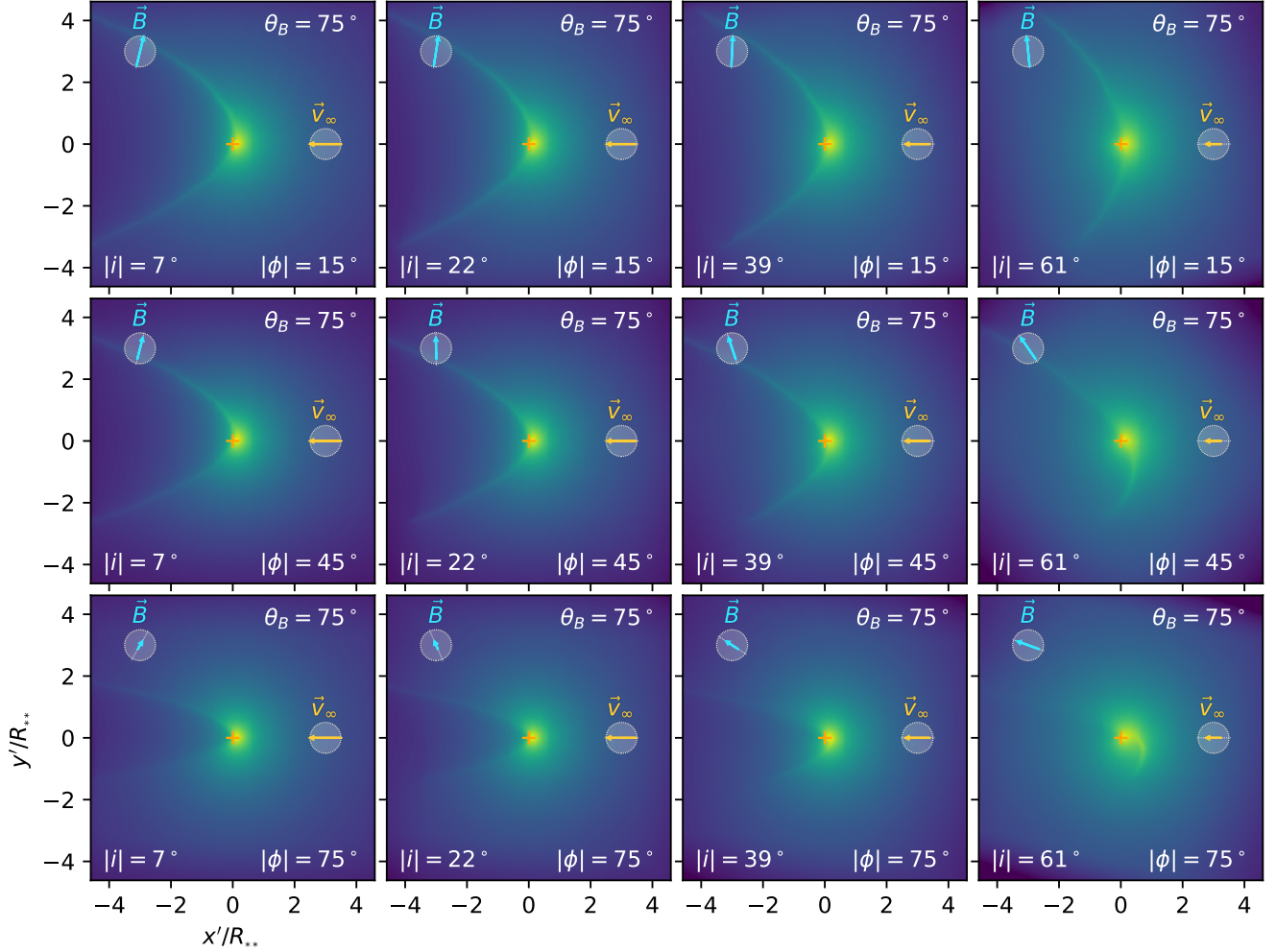


Figure D4. xxx

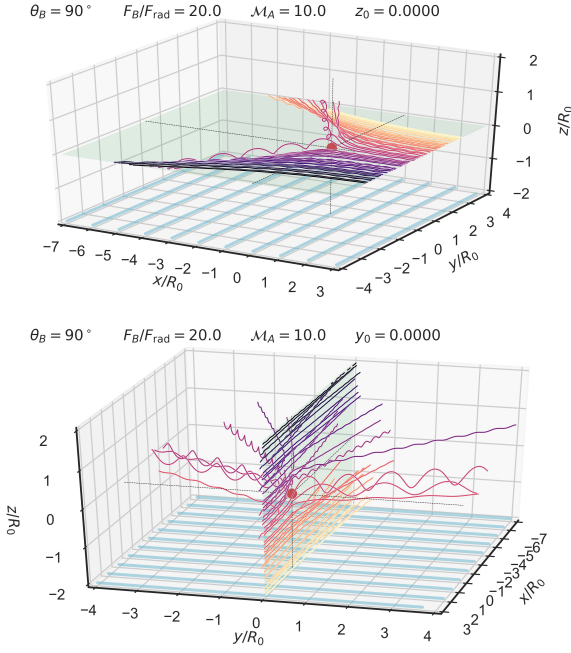


Figure D5. Streamlines in three dimensions of resolved gyro-radius

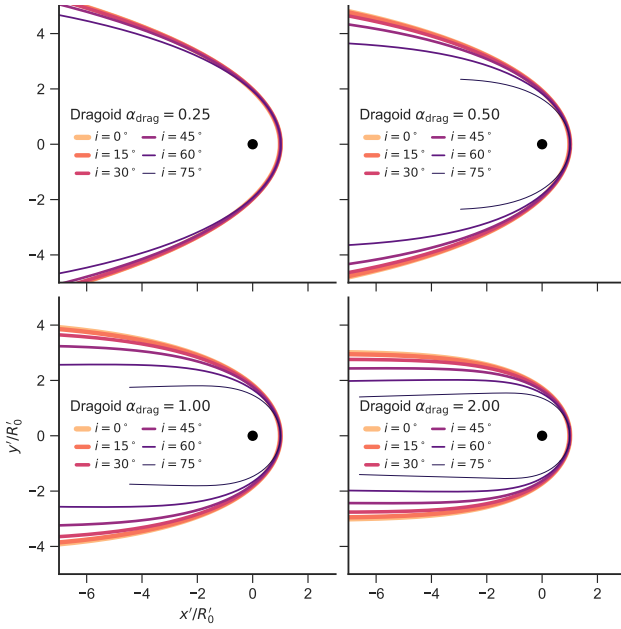


Figure F1. Apparent bow shapes in the plane of the sky for parallel-stream dragoids as a function of inclination angle. Drag coefficient, α_{drag} increases from top-left to bottom-right. Inclination $|i|$ is shown in 15° increments, indicated by line color and thickness (see key).

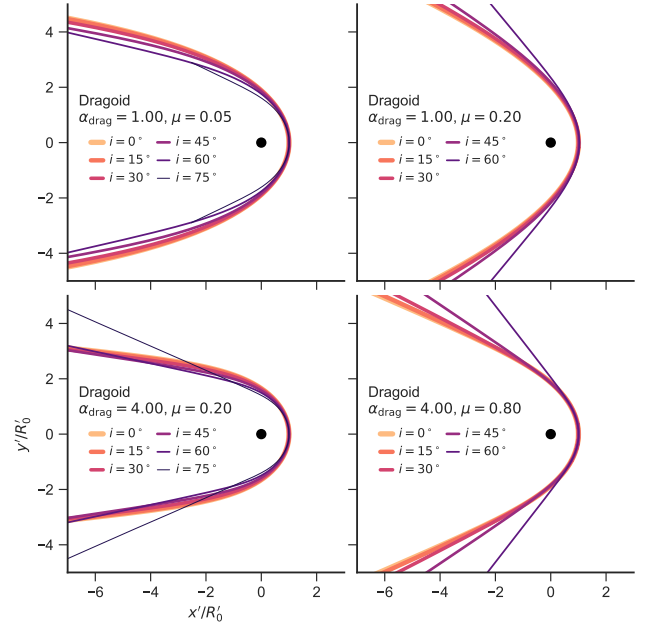


Figure F2. As Fig. F1 but for divergent stream dragoids. Drag coefficient increases from top to bottom, while degree of divergence increases from left to right.

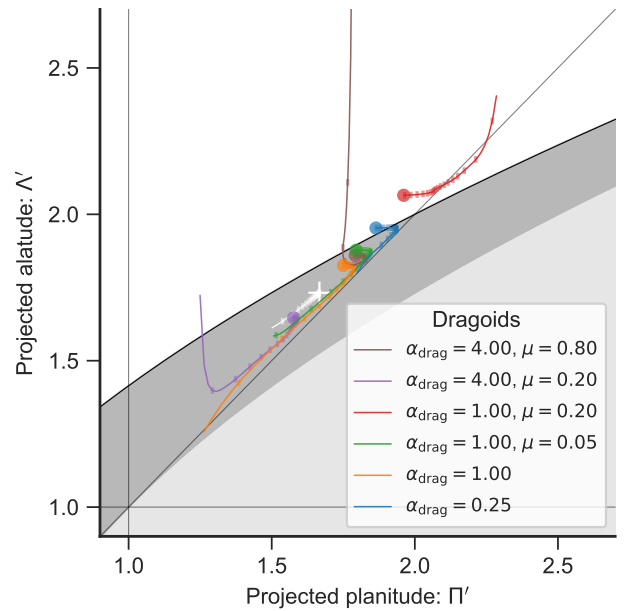
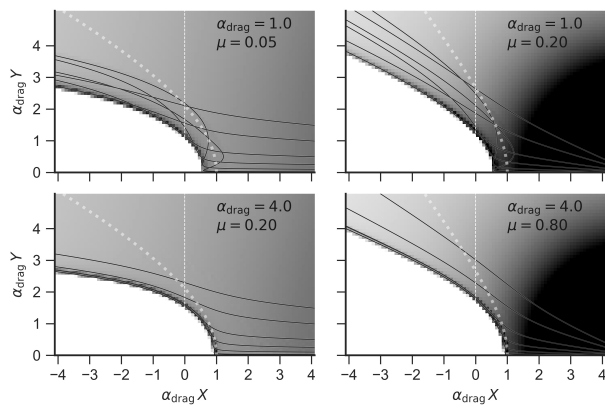


Figure F3. Apparent projected shapes of dragoids in the Π' – Λ' plane. Colored symbols indicate the $|i| = 0$ position for selected models (see key). Thin lines show the inclination-dependent tracks of each model, with tick marks along each track for 20 equal-spaced values of $|\sin i|$. Gray shaded regions are as in Fig. 11a of Paper I. The wilkinoid track is shown in white.

**Figure H1.** Divergent dragoids